Journal of Hazardous Materials 408 (2021) 124830

Contents lists available at ScienceDirect

Journal of Hazardous Materials

journal homepage: www.elsevier.com/locate/jhazmat

Research paper

Highly efficient simultaneous removal of HCHO and elemental mercury over Mn-Co oxides promoted Zr-AC samples

Xueyu Du [a,b], Caiting Li [a,b,*], Jie Zhang [a,b], Lingkui Zhao [c], Shanhong Li [a,b], Yue Lyu [a,b], Yindi Zhang [a,b], Youcai Zhu [a,b], Le Huang [a,b]

[a] *College of Environmental Science and Engineering, Hunan University, Changsha 410082, PR China*
[b] *Key Laboratory of Environmental Biology and Pollution Control (Hunan University), Ministry of Education, Changsha 410082, PR China*
[c] *College of Environment and Resources, Xiangtan University, Xiangtan 411105, PR China*

ARTICLE INFO

Editor: Dr. H. Zaher

Keywords:
HCHO
Hg^0
Simultaneous removal
Zr-AC
Mn-Co oxides

ABSTRACT

Mn_xCo_y/Zr_z-AC prepared by impregnation method was investigated on the simultaneous removal of HCHO and Hg^0. The samples were characterized by BET, SEM, XRD, H_2 pulse chemisorption, H_2-TPR, XPS, Hg-TPD and in-situ DRIFTS. Thereinto, the optimal $Mn_{2/3}Co_8/Zr_{10}$-AC achieved 99.87% HCHO removal efficiency and 82.41% Hg^0 removal efficiency at 240 °C, respectively. With increased surface area and pore volume, Zr-AC support facilitated higher dispersion of MnO_x-CoO_x. Moreover, the co-doping of MnO_x-CoO_x endowed the sample with more active oxygen species and higher reducibility, which further facilitated the removal of HCHO and Hg^0. Chemisorption was proved to predominate in Hg^0 removal, and oxidation also worked as Hg^{2+} was detected in outlet gas. Besides, HCHO predominated in the competition of active oxygen species, especially for lattice oxygen, thus suppressed the Hg^0 removal. According to in-situ DRIFTS, HCHO removal proceeded as $HCHO_{ads} \rightarrow$ DOM → formate species → $CO_2 + H_2O$, and was boosted by active oxygen species. Furthermore, $Mn_{2/3}Co_8/Zr_{10}$-AC was proved with excellent regeneration performance, indicating its potential in practical application.

1. Introduction

With the implementation of ultra-low emission since 2014, the emission of SO_2 and NO_x from coal-fired power plants has been controlled effectively in China (Wang and Zhang, 2019). Volatile organic compounds (VOCs) and mercury, following with SO_2, NO_x and particulate matter (PM), have gained more and more emphasis in recent decades due to their high volatility, chemical stability and accumulation (Chi et al., 2017; Gelles et al., 2020). As one of the largest anthropogenic mercury emission source, coal combustion also contributed to 0.24 Tg VOCs, and accounted for almost 1.1% of total VOCs emission in China in 2010, which were mainly consisted of aldehydes (formaldehyde and acetaldehyde), alkanes and alkenes, aliphatic and aromatic hydrocarbons (toluene, xylenes, ethylbenzene and benzene) and chlorinated hydrocarbons (Garcia et al., 1992; Yan et al., 2016; Liu et al., 2020). Besides posing a great threat to human health, these pollutants are also responsible for a wealth of air pollutions, such as the formation of secondary organic aerosol with high toxicity due to their adhesion to PM, the photochemical smog and haze (Du et al., 2018b; Zhao et al., 2018). In particular, HCHO, with the intrinsic "irritant-teratogenic-carcinogenic" effect, is listed as the second toxics that should be preferentially controlled in China (He and Ji, 2010; He et al., 2019a). Different from particle bound mercury (Hg^P) and oxidized mercury (Hg^{2+}), elemental mercury (Hg^0) possesses high volatility and low water solubility, thus is regarded as the key of mercury removal (Zeng et al., 2017). However, there is the lack of mature technologies for the removal of VOCs and Hg^0. To further reduce the air pollution, effective and promising technology for VOCs and Hg^0 elimination should also be taken into account to meet more restrictions for VOCs and mercury emissions (Yang et al., 2019; Zhou and Diao, 2020).

To date, various technologies, including adsorption (Yu et al., 2013; Wu et al., 2015), catalytic oxidation (Liu et al., 2016; Zhao et al., 2016), photocatalytic oxidation (Chen et al., 2014; Zhang et al., 2014), plasma removal (An et al., 2014; Zhu et al., 2016) and so on, have been investigated on the individual removal of HCHO and Hg^0. However, there still exist some problems, such as limited adsorption capacity, high reaction temperature required and the generation of harmful byproducts, for aforementioned technologies (Yu et al., 2013). Alternatively,

---

* Corresponding author at: College of Environmental Science and Engineering, Hunan University, Changsha 410082, PR China.
E-mail address: ctli@hnu.edu.cn (C. Li).

https://doi.org/10.1016/j.jhazmat.2020.124830
Received 10 October 2020; Received in revised form 3 December 2020; Accepted 9 December 2020
Available online 15 December 2020
0304-3894/

considering the environmental friendliness and energy saving, the combination of adsorption and catalytic oxidation is highly desirable for HCHO and Hg^0 elimination.

At present, the most widely used adsorbents and catalysts are mainly in the forms of powders and particles with smaller size (Zhou et al., 2017; Yi et al., 2018). Although obtaining a higher contact area with gas reactants and thus an enhanced removal performance, the application of such adsorbents and catalysts are still restricted by the difficulty in the following dust removal apparatus and regeneration for the powders, as well as inevitable aggregation of the particles (Yu et al., 2013; Qin et al., 2017). To overcome the barriers mentioned above, cylindrical activated coke (AC) materials come into consideration. As a carbonaceous material, AC not only has the affinity for activated carbon, which possesses various surface functional groups and tunable porous structure, but also exhibits superiority in practical industrial application due to its higher mechanical strength, better regeneration performance and lower cost than activated carbon and some other mineral materials (Zhao et al., 2016; Zhu et al., 2020). And with more mesopores and macropores, AC is regarded as better support for loading active components and superior adsorbent for macromolecules. Besides, the hydrophobicity of AC prevents the sample from H_2O-poisoning when applied in the flue gas containing water vapor (Wu et al., 2015). As a result, AC has been investigated as the efficient adsorbents/catalysts for the removal of SO_2, H_2S, NO_x, Hg^0 and VOCs (Zhao et al., 2016; Qie et al., 2020). Herein, AC was chosen for the removal of VOCs and Hg^0 on the basis of existing desulfurization and denitration device using activated coke, which was beneficial for the cost saving and maintenance of equipment in practical application. However, as the decisive factors of the adsorption capacity and catalytic activity, different pore structures and surface functional groups of AC were desired when treating diverse air pollutants (Fang et al., 2017). Generally, the limited surface functional groups and pore structure of virgin AC could not always meet the need for the efficient removal of diverse air pollutants. Therefore, it is important to explore how to adjust and improve the property of AC to some extent. As reported, loading with noble metal or transition metal oxides could endow the carbon-based materials with an increased adsorption and oxidation capacity through the optimization of its physicochemical properties (Chen et al., 2018). Hence, modifying AC with transition metal oxides, with lower cost and stronger resistance to chlorine poisoning superior to noble metal, seems to be the practicable approach to enhance the activity of AC (Piumetti et al., 2015).

Among the transition metal oxides, manganese oxide revealed excellent activity in the elimination of Hg^0 (Li et al., 2020), CO (Ma et al., 2019), hydrocarbon (Finocchio and Busca, 2001), aromatic (Wang et al., 2021) and Cl-VOCs (Kan et al., 2017). On one hand, as an oxygen storage material, manganese oxides could generate abundant active oxygen species through the valence states transformation (Du et al., 2018a). On the other hand, the variable valences of manganese contribute to the electrons of manganese oxides with high mobility, which could provide the mobile-electron environment to facilitate the catalytic reaction (Liang et al., 2016). Nevertheless, the application of manganese oxides was still limited by its lower resistance to SO_2 poisoning in practical industry (Jiang et al., 2016). According to previous researches, the incorporation of cobalt oxides could weaken the SO_2 adsorption strength on the catalyst surface, and conduce to an enhanced SO_2 resistance (Jiang et al., 2018). Moreover, Kan et al. (2017) demonstrated that the Co doping contributed to the generation of more lattice defects and oxygen vacancies, which gave rise to higher oxygen mobility. Meanwhile, the Mn-Co co-doping catalysts could provide more active oxygen species in the removal of HCHO and Hg^0 due to the storage and release of oxygen through the synergy between $Mn^{4+}/Mn^{3+}/Mn^{2+}$ and Co^{3+}/Co^{2+} couples. Therefore, modifying with Mn-Co oxides should be feasible to endow the AC with effective removal of HCHO and Hg^0.

In addition, the dispersion of active components doped was also considered to be of utmost importance for the physico-chemical properties of samples, including the surface area, morphology structure and reducibility, which determined the activity (Zhu et al., 2013). In general, more highly-dispersed the metal oxides are, higher activity the sample possesses. However, there is always the agglomeration of active components formed on AC surface when loaded with a higher content of metal oxides (Du et al., 2018a). In this respect, zirconium oxide, as n-type semiconductor, arouses wide concerns because of its applicability in the improvement of surface area of support and dispersion of active components (Huang et al., 2013b). Wang et al. (2017) prepared the $CuO-CeO_2/TiO_2-ZrO_2$ for simultaneous removal of Hg^0 and NO, and the results indicated that the doping of ZrO_2 on support of $CuO-CeO_2/TiO_2$ could benefit the great surface area and weakened crystallinity of TiO_2, and then improved the dispersion of metal oxides. And Agrell et al. (2003) found that the ZrO_2 prevented the sintering of Cu crystallites effectively, and endowed the catalysts with a higher thermal stability. Moreover, ZrO_2 is also a promising promoter due to its enhancement on reducibility and oxygen storage capacity, which facilitates its potential in practical application (Sato et al., 2013). Unfortunately, to the best of our knowledge, ZrO_2-doped AC with high surface area as the support for mixed Mn-Co oxides has been rarely investigated for the simultaneous removal of HCHO and Hg^0.

In this study, MnO_x-CoO_x supported on ZrO_2-doped AC was prepared for the simultaneous removal of HCHO and Hg^0. The effect of ZrO_2 and MnO_x-CoO_x addition on the activity of AC sample was addressed. The correlation between the activity of Mn_xCo_y/Zr_z-AC and surface chemical property, textural and structural characteristic was also investigated by numerous characterizations, including BET, SEM, XRD, H_2 pulse chemisorption, H_2-TPR and XPS. In addition, the mechanism of HCHO and Hg^0 removal over Mn_xCo_y/Zr_z-AC, as well as the interaction between HCHO and Hg^0, were also proposed with the aid of in-situ DRIFTS and Hg-TPD.

2. Experimental

2.1. Sample preparation

The Mn_xCo_y/Zr_z-AC samples were synthesized by stepwise equivalent volume impregnation method. The AC was firstly doped with ZrO_2, and followed by the impregnation of MnO_x-CoO_x. Thereinto, x was denoted as the molar ratio of Mn/(Mn+Co) in the range of 0–1, and y and z, set as 0–10, presented the mass percent of Mn-Co oxides and ZrO_2 on sample, respectively. For example, 3.0330 g $Zr(NO_3)_4 \cdot 5H_2O$, 1.5913 mL 50 wt% $Mn(NO_3)_2$ solution and 0.9949 g $Co(NO_3)_2 \cdot 6H_2O$ were dissolved into deionized water for 20 g virgin AC to prepared $Mn_{2/3}Co_4/Zr_4$-AC. Please refer to the synthesis of Mn_xCo_y/Zr_z-AC in the Supporting Information for further details.

2.2. Characterization of samples

The prepared samples were characterized by numerous technologies, including N_2 adsorption-desorption, scanning electron microscopy (SEM), X-ray diffraction (XRD), H_2 pulse chemisorption, H_2 temperature-programmed reduction (H_2-TPR), X-ray photoelectron spectroscopy (XPS), mercury temperature-programmed desorption (Hg-TPD), and in situ diffuse reflectance infrared Fourier transform spectroscopy (in-situ DRIFTS). More detailed characterization methods are provided in the Supporting Information.

2.3. Experimental setup and procedure

As shown in Fig. 1, the continuous-flow fix-bed reactor was used to evaluate the simultaneous removal performance of HCHO and Hg^0 over Mn_xCo_y/Zr_z-AC, which included a simulated flue gas supplying system, a reactor section, and a reaction gas analyzing system. Gaseous HCHO was generated by a peristaltic pump to inject 38 wt% formaldehyde solution into polytef tube wrapped with heating tape. Before mixed with other

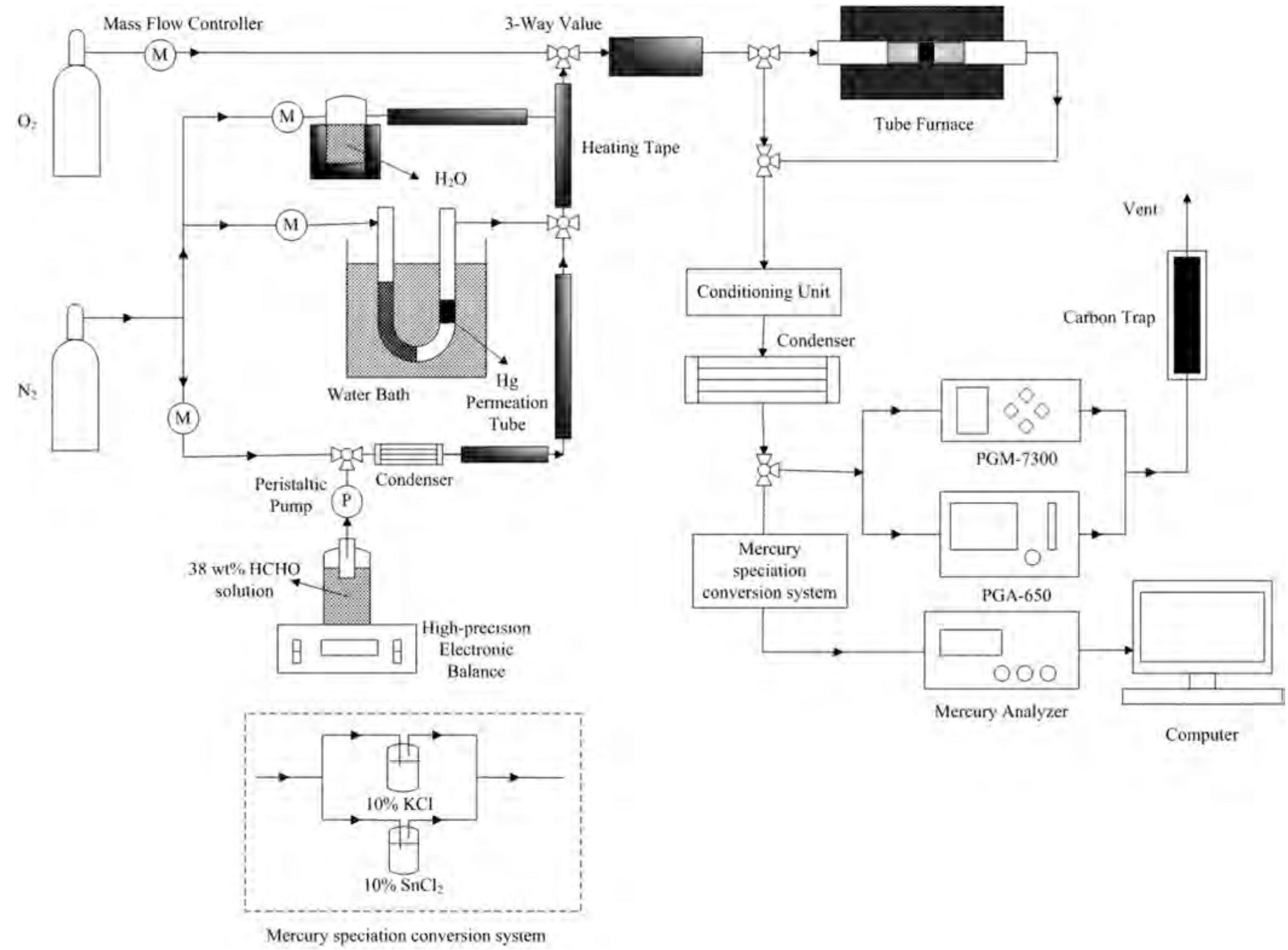

Fig. 1. Schematic diagram of the experimental setup.

gas components, the gas-phase HCHO was carried by 100 mL/min N_2 through the condenser to blow the water vapor off. An elemental mercury permeation tube (VICI Metronics, USA) placed in a temperature-controlled water bath was used to generate Hg^0 vapor with 100 mL/min high purity N_2 as the carrier gas. 20 g sample was placed into a quartz tube (ID = 55 mm), which was inserted into a temperature-programmed tube furnace, under an atmosphere consisting of 100.0 ± 0.5 μg/m^3 Hg^0, 120.0 ± 2.0 ppm HCHO, 0–6% O_2, 0–8 vol% H_2O and balanced N_2. Besides, all gas flows were controlled by mass flow controllers at a total flow rate of 500 mL/min, corresponding to a gas hourly space velocity (GHSV) of 3000 h^{-1} that was higher than the practical GHSV used in activated coke tower. An online RA-915M mercury analyzer (LUMEX Ltd, Russia) was employed to monitor the concentration of Hg^0 continuously. The concentration of inlet and outlet HCHO was measured using PGM7340 analyzer (RAE, USA), and a PGA-650 analyzer (Phymetrix, USA) was used to detect the concentration of CO_2 resulting from the oxidation of HCHO. At the beginning of the test, the desired concentration of HCHO and/or Hg^0 was detected to keep stable for 30 min, and then the simulated flue gas was introduced to pass through the sample for 6 h. And all experiments were repeated for three times to ensure the accuracy and reliability of experimental results. In particular, a blank test was conducted to eliminate any interference of the reactor.

The HCHO removal efficiency (E_{HCHO}) and CO_2 selectivity (S_C) was calculated by the following equations:

$$E_{HCHO}(\%) = \frac{\Delta HCHO}{HCHO_{in}} = \frac{HCHO_{in} - HCHO_{out}}{HCHO_{in}} \times 100\% \tag{1}$$

$$S_C(\%) = \frac{CO_2}{HCHO_{in} - HCHO_{out}} \times 100\% \tag{2}$$

where $HCHO_{in}$ and $HCHO_{out}$ represents the inlet and outlet concentration of HCHO, respectively. In all case, the carbon balance was near 100%.

The reaction rates of HCHO conversion were calculated to compare the catalytic activity of samples. However, it's hard to determine the accurate amount of surface active sites. Hence, we herein used the reaction rates with respect to the mass of Mn-Co oxides. The reaction rate (r_{HCHO}, μmol$_{HCHO}$/g/s) was denoted as

$$r_{HCHO} = \frac{HCHO_{in} \times E_{HCHO} \times Q}{m} \tag{3}$$

where Q (L/s) presents the total gas flow, and m (g) is the mass of sample used in the experiment.

The Hg^0 removal efficiency (E_T), the Hg^0 adsorption efficiency (E_{ads}) and the Hg^0 oxidation efficiency (E_{oxi}) were calculated as the equations below:

$$E_T = \frac{\Delta Hg^0}{Hg^0_{in}} = \frac{Hg^0_{in} - Hg^0_{out}}{Hg^0_{in}} \times 100\% \tag{4}$$

$$E_{ads} = \frac{Hg^0_{in} - Hg^T_{out}}{Hg^0_{in}} \times 100\% \quad (5)$$

$$E_{oxi} = \frac{Hg^{2+}}{Hg^0_{in}} = \frac{Hg^T_{out} - Hg^0_{out}}{Hg^0_{in}} \times 100\% \quad (6)$$

$$E_T = E_{ads} + E_{oxi} \quad (7)$$

where Hg^0_{in} and Hg^0_{out} is the Hg^0 concentration detected in the inlet flue gas and outlet flue gas, respectively. Besides, the Hg^{2+} in the outlet gas was measured by the mercury speciation conversion system, in which resulted Hg^{2+} could be converted into Hg^0 by 10% $SnCl_2$ solution as reductant (Zeng et al., 2017). And Hg^T_{out} was the outlet concentration of Hg^0 passed through the mercury speciation conversion system.

To estimate the regeneration performance of sample, recycle experiment was conducted with a higher GHSV of 6000 h^{-1}. After treated with the feed gas for 4 h, the sample was heated at 400ºC under pure N_2 for 1 h. When the reactor was cooled down to 240 °C, another cycle was started under the same treatment condition. And the recycle test was repeated for five cycles. Additionally, the abatement of HCHO and Hg^0 was expressed as the ratio of outlet (C) and inlet (C_0) concentration (C/C_0), respectively.

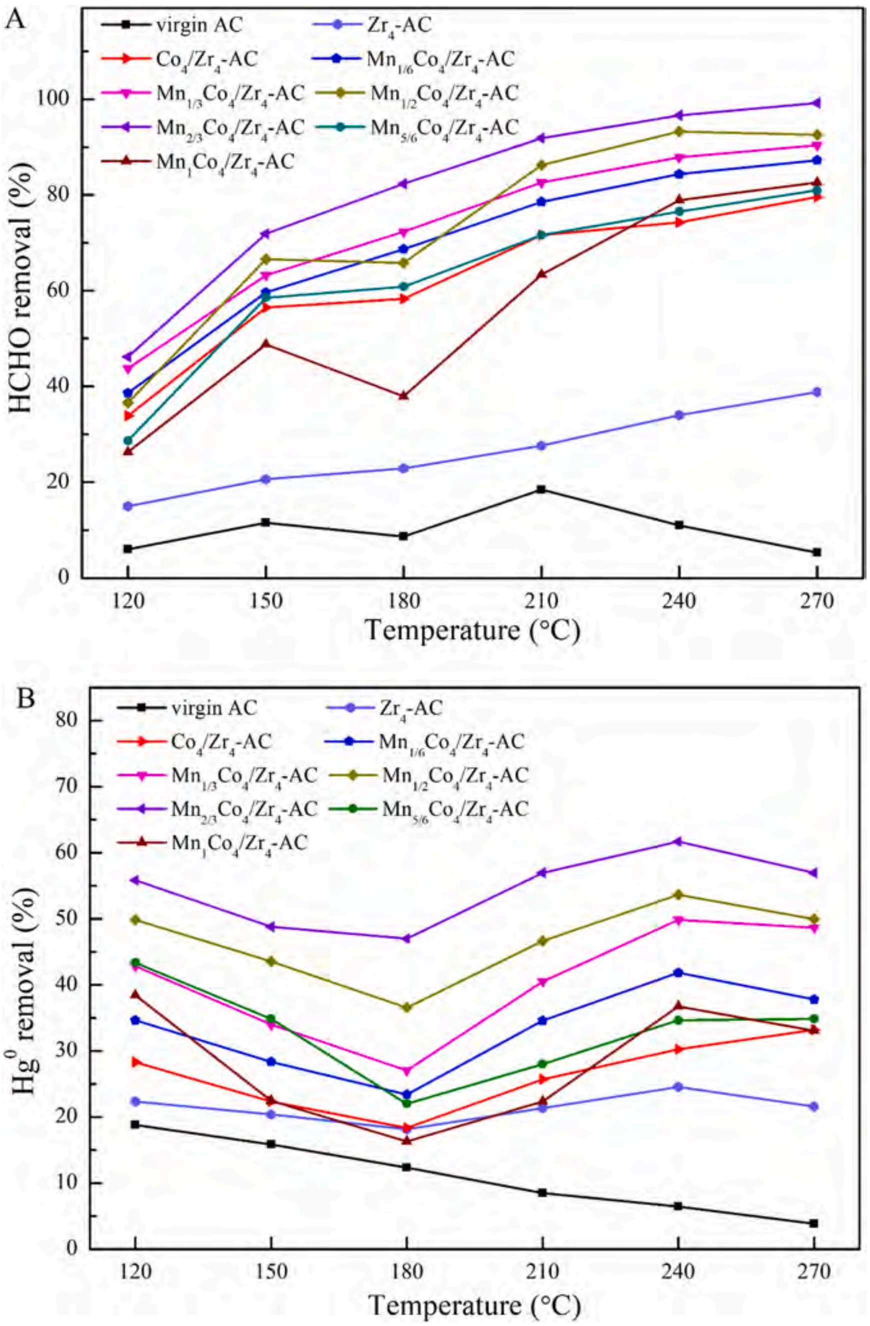

Fig. 2. The performance of simultaneous removal of (A) HCHO and (B) Hg^0 over virgin AC, Zr_4-AC and Mn_xCo_4/Zr_4-AC samples (Reaction condition: 120 ppm HCHO, 100 μg/m^3 Hg^0, 6% O_2, 8 vol% H_2O, total flow rate 500 mL/min, 20 g sample, reaction temperature 120–270 °C).

3. Results

3.1. Catalytic performance

3.1.1. Effect of molar ratio of Mn/(Mn+Co)

The dependences of HCHO and Hg^0 removal on reaction temperature for simultaneous removal of HCHO and Hg^0 over virgin AC, Zr_4-AC and Mn_xCo_4/Zr_4-AC were investigated in this work. As depicted in Fig. 2, the removal performance of virgin AC was firstly investigated, and only lower than 18.47% and 18.81% for HCHO and Hg^0 removal efficiency was reached at the whole temperature window, respectively. In contrast, both the dopant of ZrO_2 on AC support and the further incorporation of MnO_x-CoO_x on Zr-AC outstandingly accelerated the removal of both HCHO and Hg^0. It was noticed that both HCHO and Hg^0 removal were influenced by the molar ratio of Mn/(Mn+Co) to a large extent, which exhibited a growth trend and then decreased sharply with increasing molar proportion of MnO_x. Obviously, the co-impregnated Zr_4-AC owned the activity superior to single metal oxide modified Zr_4-AC, highlighting the beneficial synergy between MnO_x and CoO_x. Thereinto, $Mn_{2/3}Co_4/Zr_4$-AC, with Mn/(Mn+Co) molar ratio of 2/3, exhibited the highest HCHO and Hg^0 removal efficiency at the overall tested temperature window. On the other hand, diverse trends changing with reaction temperature were observed for HCHO and Hg^0 removal on Mn_xCo_4/Zr_4-AC. HCHO removal showed a general positive correlation with reaction temperature. After an initial decrease, the activity for Hg^0 removal increased until the temperature elevated up to 240 °C, and the further increased temperature led to a slight deterioration. Notably, compared with lower temperature, the positive effect of co-modification on activity became more evident at higher temperature for both HCHO and Hg^0 removal. Therefore, 240 °C was chose as the optimal temperature for the simultaneous removal of HCHO and Hg^0 over Mn_xCo_y/Zr_z-AC.

Interestingly, Co_4/Zr_4-AC possessed higher removal efficiency than Mn_1Co_4/Zr_4-AC at lower temperature, while the activity of Mn_1Co_4/Zr_4-AC was superior to that of Co_4/Zr_4-AC when temperature elevated to 240 °C. As demonstrated by Piumetti et al., only the surface adsorbed oxygen of catalyst might reach the equilibrium with the gas-phase oxygen at low temperature; as temperature rose, the bulk oxygen, instead of the outer layer of catalyst, would exchange with gas-phase oxygen (Chen et al., 2018). Therefore, the bulk oxygen in Mn_1Co_4/Zr_4-AC might be easier to be activated than that of Co_4/Zr_4-AC, and the surface oxygen of Co_4/Zr_4-AC might be more active. In conclusion, the synergy between active oxygen species of MnO_x and CoO_x should be responsible for the superior catalytic activity of Mn_xCo_4/Zr_4-AC ($0 < x < 1$), and it will be discussed in detail afterwards.

3.1.2. Effect of loading value

The content of active components is relevant to the dispersion, aggregation and crystallinity of metal oxides over support, as well as its redox property (Zhu et al., 2013). As illustrated in Fig. 3, the effects of the loading value of Mn-Co oxides and ZrO_2 on simultaneous removal of HCHO and Hg^0 were investigated, respectively. In terms of $Mn_{2/3}Co_y/Zr_4$-AC series samples, the modification of 4% ZrO_2 on AC led to an increase of 23.02% and 18.12% for HCHO and Hg^0 removal compared with virgin AC, respectively, indicating the significant promotion effect of ZrO_2. As the loading value of Mn-Co oxides increased, the HCHO removal efficiency increased with a decreased growth rate, especially when $y > 4$. However, the curve of Hg^0 removal efficiency reached the maximum of 71.85% for $Mn_{2/3}Co_8/Zr_4$-AC and then decreased. When investigating the catalytic activity of $Mn_{2/3}Co_8/Zr_z$-AC, both HCHO and Hg^0 removal possessed a positive correlation with the loading value of ZrO_2. Among all examined samples, $Mn_{2/3}Co_8/Zr_{10}$-AC possessed the highest activity with 99.87% HCHO removal efficiency and 82.41% Hg^0 removal efficiency at 240 °C, respectively. Moreover, to probe into the inherent activity of $Mn_{2/3}Co_8/Zr_{10}$-AC, physical mixture of Mn-Co oxides and Zr_{10}-AC was prepared as comparative sample. As shown in Fig. S1, with the same content of active components, both HCHO and Hg^0 removal efficiency of physical mixture were lower than half of those on $Mn_{2/3}Co_8/Zr_{10}$-AC, indicating the existence of strong metal oxides-support interaction (SMSI).

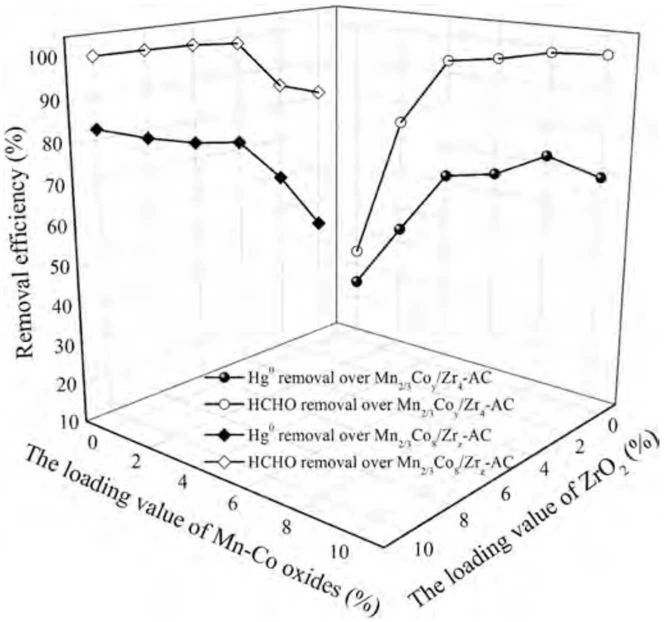

Fig. 3. The catalytic activity of $Mn_{2/3}Co_y/Zr_4$-AC and $Mn_{2/3}Co_8/Zr_z$-AC samples in the simultaneous removal of HCHO and Hg^0 (Reaction condition: 120 ppm HCHO, 100 μg/m^3 Hg^0, 6% O_2, 8 vol% H_2O, total flow rate 500 mL/min, 20 g sample, reaction temperature 240 ℃).

3.1.3. Effect of O_2 and H_2O

High removal efficiency is not the only criterion to identify effective adsorbent-catalyst for simultaneous removal of HCHO and Hg^0. In addition, whether the desired reaction pathway has proceeded also should be taken into consideration, where O_2 and H_2O play an essential role for both adsorption and oxidation (Yi et al., 2018). Inevitably, the removal performance, especially the oxidation, of HCHO and Hg^0 over $Mn_{2/3}Co_8/Zr_{10}$-AC was conducted with different O_2 concentration at 60–270 °C. As shown in Fig. 4, under pure N_2, both the removal of HCHO and Hg^0 on $Mn_{2/3}Co_8/Zr_{10}$-AC were mainly in the form of adsorption at lower temperature, and the oxidation gradually strengthened with the increasing temperature, especially for HCHO removal. In general, the injection of 8 vol% H_2O significantly facilitated the CO_2 selectivity and HCHO removal efficiency, except for the weakened HCHO removal efficiency at 60–90 °C resulted from the competitive adsorption between HCHO and H_2O. Conversely, the competition for the active sites dominated in the Hg^0 removal with the presence of 8 vol% water, while a mild enhancement on Hg^0 oxidation was also detected. The positive effect of H_2O addition might be due to the generation of hydroxyl groups via the its dissociation on saturated sites. As reported, the hydroxyl radical (–OH) from water vapor could not only make for the quick oxidation HCHO via adsorbing at the vicinity of active sites, but also directly act as the active sites for the HCHO adsorption and the subsequent oxidation into formate species (Chen et al., 2019; Yan et al., 2019). In addition, the stimulative desorption of products, such as CO_2, with the aid of additive water and surficial –OH also worked during enhanced HCHO removal (Wang et al., 2018). Likewise, oxidation of Hg^0 by the formed -OH might be responsible for the slightly enhanced E_{oxi}. Besides the facilitation on the generation of –OH expressed as $O_2 + H_2O \rightarrow O^* + 2OH$, the presence of O_2 could generate the lattice oxygen and replenish the chemisorbed oxygen consumed during reaction, as demonstrated by the highest activity in term of simultaneous removal of HCHO and Hg^0 with the co-existence of

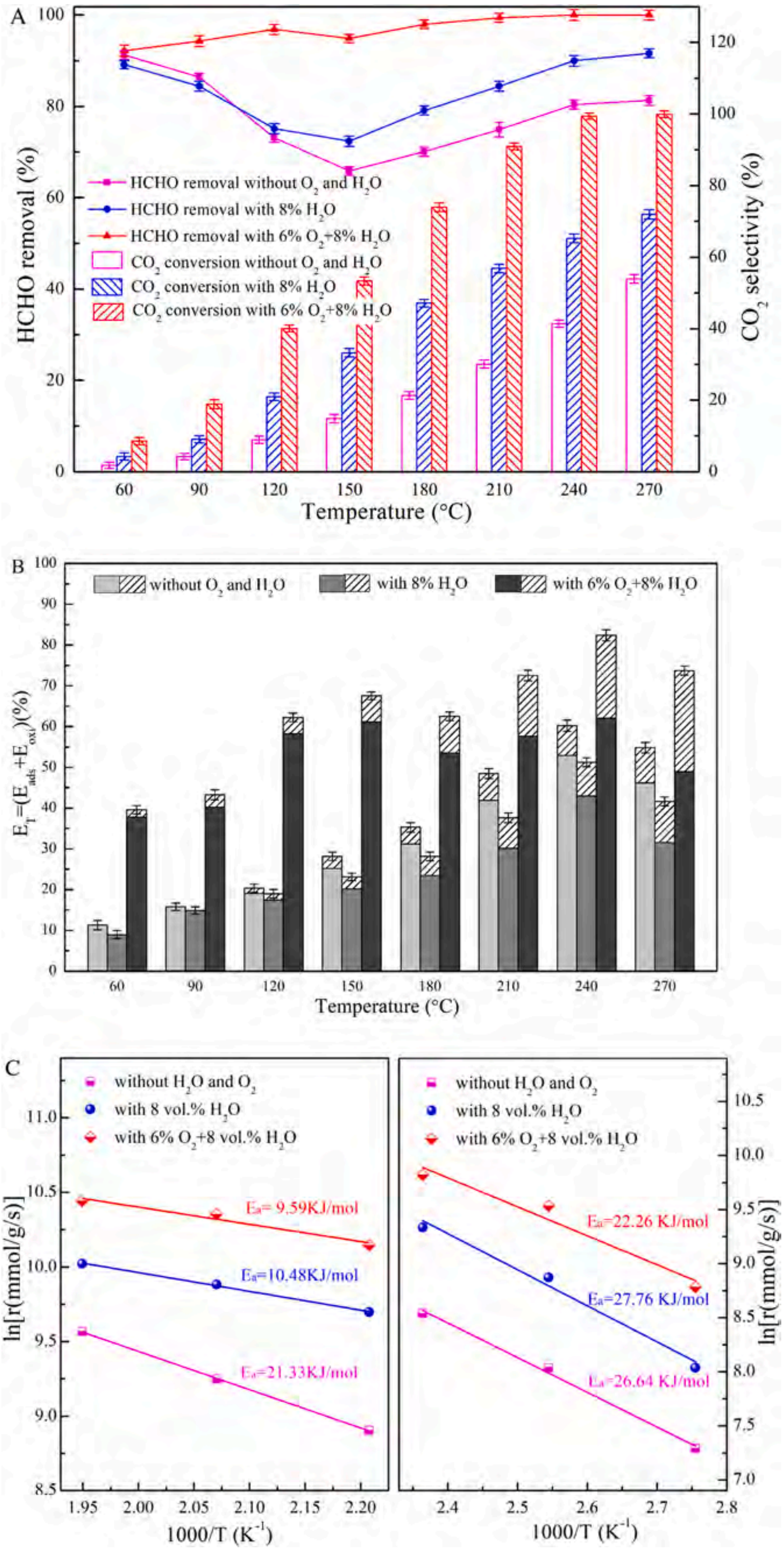

Fig. 4. (A) HCHO removal and (B) Hg^0 removal, where Hg^0 adsorption and Hg^0 oxidation was presented by the column filled with solid color and the column filled with oblique line, respectively, over $Mn_{2/3}Co_8/Zr_{10}$-AC as a function of the reaction temperature in simulated flue gas with different O_2 and H_2O concentration, and the error bars in (B) were for E_T. (C) Arrhenius plots of HCHO oxidation at different temperature over $Mn_{2/3}Co_8/Zr_{10}$-AC (Reaction condition: 120 ppm HCHO, 100 μg/m^3 Hg^0, 0–6% O_2, 0–8 vol% H_2O, total flow rate 500 mL/min, 20 g sample, reaction temperature 60–270 °C).

6% O_2 + 8 vol% H_2O (Du et al., 2018a).

The acceleration of H_2O and O_2 is also reflected in the activation energies (Ea) measured in lower temperature range (90–150 °C) and higher temperature range (180–240 °C), which was calculated according to the slopes of Arrhenius plots of HCHO oxidation. As shown in Fig. 4C, the addition of 6% O_2 + 8 vol% H_2O decreased the Ea from 26.64 KJ/mol to 22.26 KJ/mol at lower temperature, and the decrease became more apparent at higher temperature. This is consistent with the performance test showing that the promotion effect of H_2O and O_2 on the activity of $Mn_{2/3}Co_8/Zr_{10}$-AC was strengthened with increasing reaction temperature. Interestingly, although the presence of 8 vol% H_2O resulted in the decrease of Ea at higher temperature, a slightly higher Ea in comparison of that under pure N_2 was detected at low temperature, which indicated that due to water vapor, the activity of sample exhibited higher sensitivity to temperature at lower temperature.

3.1.4. *Interaction between HCHO and Hg^0 removal*

As described in Fig. 5, the relationship between HCHO removal and Hg^0 removal over $Mn_{2/3}Co_8/Zr_{10}$-AC was investigated at 120–270 °C. It was clearly observed that irrespective of reaction temperature, there was only a slight decrease of HCHO removal efficiency conduced from the addition of 100 μg/m^3 Hg^0. Inversely, both Hg^0 adsorption and Hg^0 oxidation decreased sharply with additive HCHO, and more serious inhibition was observed for Hg^0 adsorption. It indicated that HCHO played a dominant role in the simultaneous removal of HCHO and Hg^0, in which HCHO, with 3-order higher concentration (120 ppm) than Hg^0 (100 μg/m^3), was in the superiority for the competition of active sites and active oxygen species. Additionally, with increasing reaction temperature, the inhibition on Hg^0 removal caused by additive HCHO was weakened. The enhanced Hg^0 oxidation as temperature rose should be responsible for it. With increasing reaction temperature, the competition between HCHO and Hg^0 transformed from adsorption sites to active oxygen species. And the addition of 6% O_2 and 8 vol% H_2O was sufficient to replenish the consumed active oxygen species. Therefore, the suppression on Hg^0 removal was obviously weakened at higher temperature.

3.2. *Textural and structural properties*

3.2.1. *Morphological structure*

Table 1 summarizes the porous structure of virgin AC and Mn_xCo_y/Zr_z-AC samples in terms of specific surface area, pore volume and average pore size. After the modification of ZrO_2, the major increase in both specific surface area and pore volume with respect to virgin AC was observed, and became more apparent with the increasing content of ZrO_2. Similar changes produced by the thermal treatment of support with $Zr(NO_3)_4{\cdot}5H_2O$ were also found in Huang's work (Huang et al., 2013b). As shown in Fig. 6A, with the modification of ZrO_2, more narrow channels were formed over virgin AC, and then gradually evolved into the spongy structure for Zr_{10}-AC (Fig. 6A(iii)), thus leading to its higher surface area. The promotional effect on specific surface area and pore volume might be ascribed to the decomposition of zirconium nitrate and chemical attract of oxygen, as well as the formation of new micropores during the calcination. Besides the increased surface area of support, there was also a lower agglomeration formed on $Mn_{2/3}Co_8/Zr_{10}$-AC due to ZrO_2 doping (Fig. 6A(iv)–(v)). Therefore, richer porous structure and higher dispersion might partly contribute to the enhanced activity of sample with ZrO_2 addition as shown in Fig. 3.

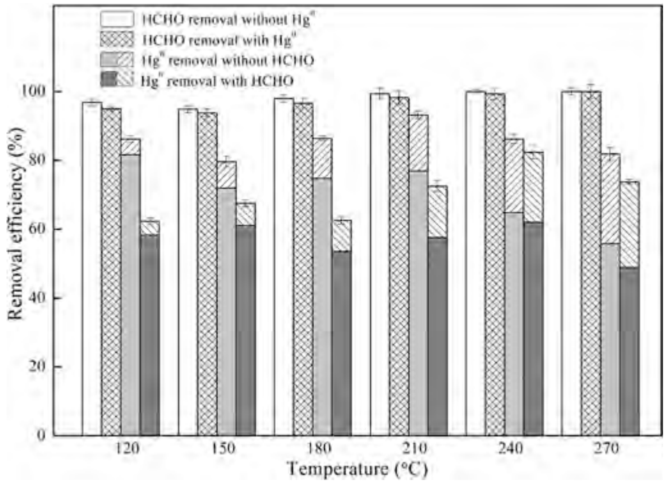

Fig. 5. The interaction between HCHO removal and Hg^0 removal over $Mn_{2/3}Co_8/Zr_{10}$-AC, where Hg^0 adsorption and Hg^0 oxidation was presented by the column filled with solid color and the column filled with oblique line, respectively (Reaction condition: 0–120 ppm HCHO, 0–100 μg/m^3 Hg^0, 6% O_2, 8 vol% H_2O, total flow rate 500 mL/min, 20 g sample, reaction temperature 120–270 ℃).

Table 1
Textural properties of virgin AC and Mn_xCo_y/Zr_z-AC samples.

Sample	BET surface area (m^2/g)	Pore volume (cm^3/g)	Pore diameter (nm)	[a]Dispersion (%)
Virgin AC	237.62	0.121	2.038	–
Zr_4-AC	269.05	0.137	2.040	–
Zr_{10}-AC	316.20	0.148	1.873	–
Co_4/Zr_4-AC	278.11	0.147	2.109	4.38
$Mn_{1/6}Co_4/Zr_4$-AC	305.33	0.145	1.905	–
$Mn_{1/3}Co_4/Zr_4$-AC	336.02	0.155	1.847	4.58
$Mn_{2/3}Co_4/Zr_4$-AC	284.50	0.145	2.037	6.67
Mn_1Co_4/Zr_4-AC	271.23	0.136	2.012	2.12
$Mn_{2/3}Co_8/Zr_{10}$-AC	288.68	0.140	1.936	–

[a] The dispersion of active metal measured by H_2 pulse chemisorption.

As shown in Table 1, the similar acceleration on surface area was also found for the impregnation of MnO_x and/or CoO_x with the loading value of 4%. Besides, the co-impregnated samples possessed higher surface area than single metal-impregnated samples, and followed this trend: $Mn_{1/3}Co_4/Zr_4$-AC > $Mn_{1/6}Co_4/Zr_4$-AC > $Mn_{2/3}Co_4/Zr_4$-AC > Co_4/Zr_4-AC > Mn_1Co_4/Zr_4-AC, which was not consistent with the order of catalytic performance. It indicated that there existed a synergy effect between metal oxides, and the surface area was not the only decisive factor for the activity of samples. What's more, $Mn_{2/3}Co_4/Zr_4$-AC showed a larger pore size than other Mn_xCo_4/Zr_4-AC samples, which could facilitate the diffusion of gas reactants into the interior of sample. Note that there was a decrease in both specific surface area and pore volume for $Mn_{2/3}Co_8/Zr_{10}$-AC as compared to Zr_{10}-AC, which might be caused by the resulting agglomeration of Mn-Co oxides and the blocking of micropores due to the entrance of Mn-Co oxides.

The strong interaction between MnO_x and CoO_x also could be revealed from SEM images. As depicted in Fig. 6B, the morphology structure of Mn_xCo_4/Zr_4-AC was affected significantly by the molar ratio of Mn/(Mn+Co). Compared with Co_4/Zr_4-AC and Mn_1Co_4/Zr_4-AC, the active components were dispersed homogeneously and existed as smaller nano-particles over co-doping samples. Notably, $Mn_{2/3}Co_4/Zr_4$-AC possessed the highest dispersion and smallest nano-particles. When it came to $Mn_{1/3}Co_4/Zr_4$-AC, a network comprising of connected robs was observed on the surface, accounting for its highest surface area among Mn_xCo_4/Zr_4-AC samples.

3.2.2. *Textural characterization*

Fig. 7A shows the XRD patterns with respect to Mn_xCo_4/Zr_4-AC with different molar ratio. For the sake of comparison, the pattern of virgin AC with the characteristic peaks ascribed to C (2θ = 26.603°, 44.464°)

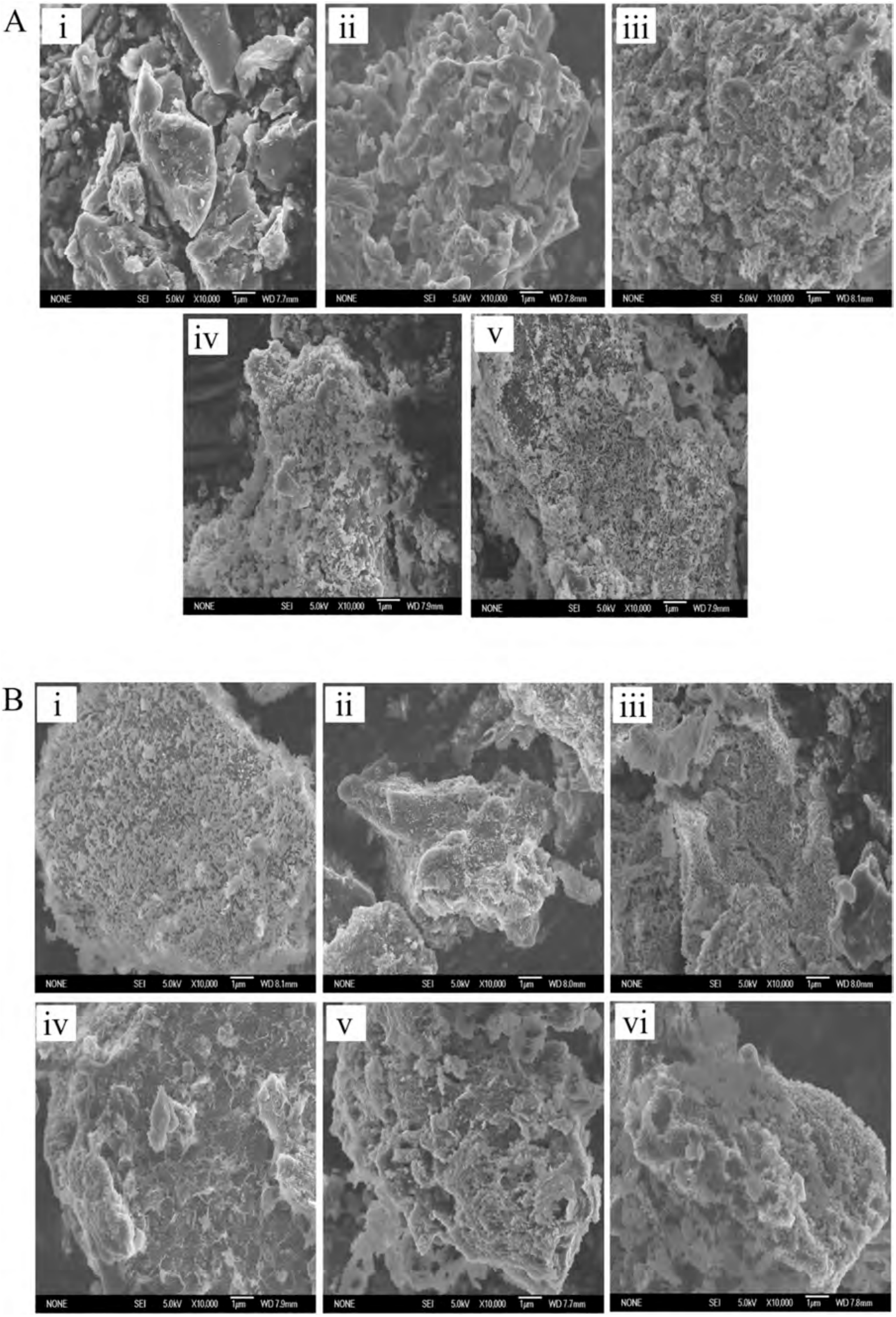

Fig. 6. (A) SEM images (×10,000) of (i) virgin AC, (ii) Zr_4-AC, (iii) Zr_{10}-AC, (iv) $Mn_{2/3}Co_8$/AC, (v) $Mn_{2/3}Co_8/Zr_{10}$-AC. (B) SEM images (×10,000) of (i) Co_4/Zr_4-AC, (ii) $Mn_{1/6}Co_4/Zr_4$-AC, (iii) $Mn_{1/3}Co_4/Zr_4$-AC, (iv) $Mn_{2/3}Co_4/Zr_4$-AC, (v) $Mn_{5/6}Co_4/Zr_4$-AC, (vi) Mn_1Co_4/Zr_4-AC.

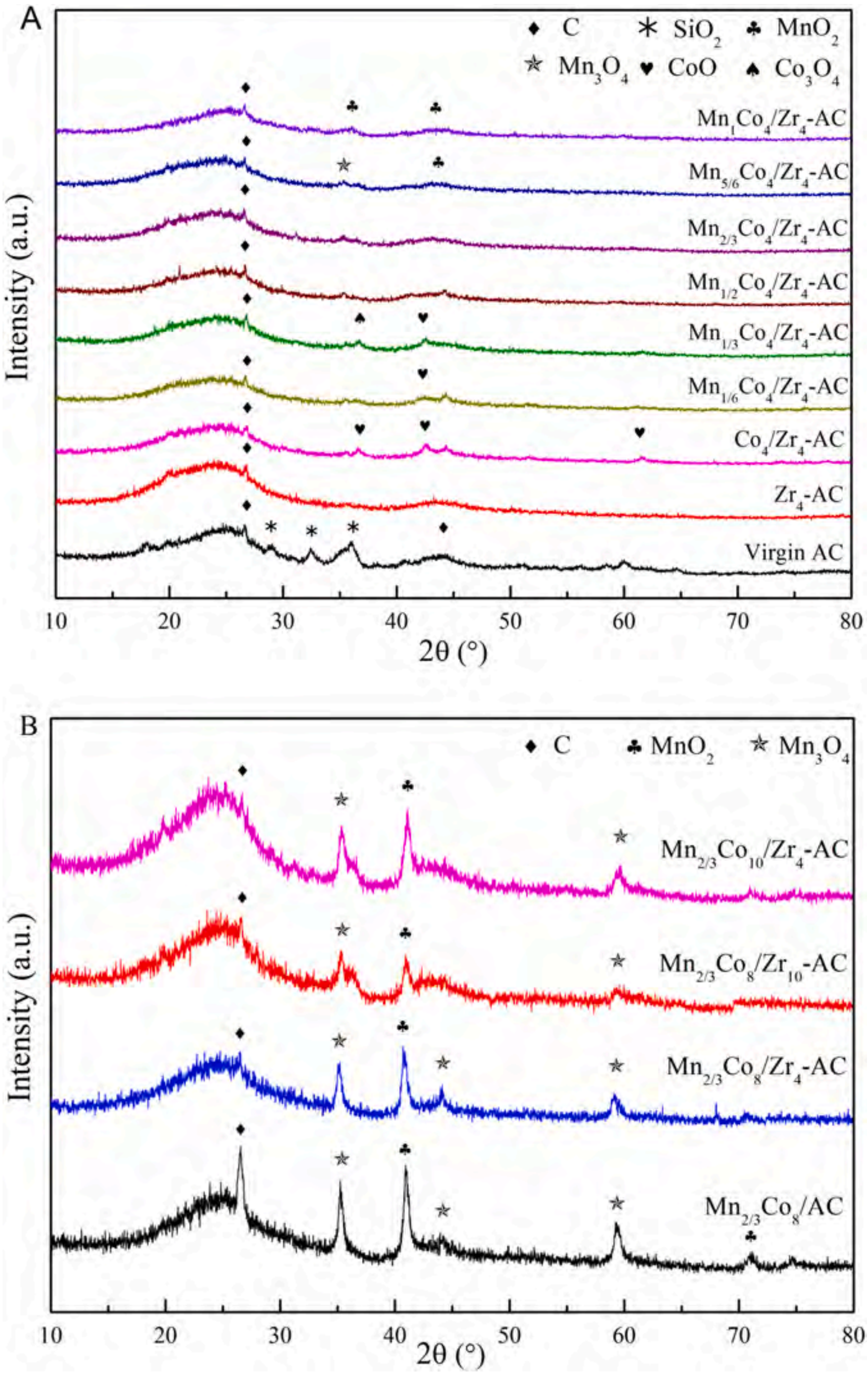

Fig. 7. XRD patterns of (A) virgin AC, Zr_4-AC and Mn_xCo_4/Zr_4-AC and (B) $Mn_{2/3}Co_y/Zr_z$-AC with different loading value of Mn-Co oxide and ZrO_2, respectively.

and SiO_2 ($2\theta = 28.899°$, $32.220°$ and $36.040°$) was also included. After the dopant of active components, only the peak at 26.603° with a weaker intensity in terms of C was observed, indicating the existence of SMSI between AC and loaded metal oxides, which was in accordance with BET and SEM. The peaks at 36.492°, 42.387° and 61.497° were observed on Co_4/Zr_4-AC, which were assigned to planet facet (111), (200) and (220) of CoO (PDF-ICDD 48-1719), respectively. Besides, for Mn_1Co_4/Zr_4-AC, the peaks at 36.883° and 43.583° were indexed to ramsdellite type MnO_2, and corresponded to the plane facet (210) and (401) (PDF-ICDD 44–0142), respectively. It was noted that the additional peaks belonged to Co_3O_4 ($2\theta = 36.852°$, with planet facet (311), PDF-ICDD 42-1467) and Mn_3O_4 ($2\theta = 36.449°$, with planet facet (202), PDF-ICDD 24-0734) were detected over $Mn_{1/3}Co_4/Zr_4$-AC and $Mn_{5/6}Co_4/Zr_4$-AC, respectively, which might be formed via the redox between MnO_x and CoO_x.

The relationship between loading value and phase composition of $Mn_{2/3}Co_y/Zr_z$-AC was also investigated by XRD, as shown in Fig. 7B. New peaks at 44.440° and 71.363° corresponding to Mn_3O_4 ((220), PDF-ICDD 24–0734) and MnO_2 ((013), PDF-ICDD 44-0142) were observed on $Mn_{2/3}Co_8/AC$. With ZrO_2 doping, most of peaks were presented with a broader range and lower intensity, and the trend became more obvious with increased ZrO_2 loading, indicating the effect of support on crystallization of Mn-Co oxides. Moreover, as revealed from Fig. 6A, $Mn_{2/3}Co_8/Zr_{10}$-AC possessed higher dispersion and lower size of active components than $Mn_{2/3}Co_8/AC$. Therefore, the broader peak meant the decrease in the crystal size, and the lower intensity proved the weakening on crystallization by ZrO_2, which has also been reported by Zhang et. al (2016). On the other hand, when increasing the loading value of Mn-Co oxides on Zr_4-AC to 10%, the peaks became more intense, indicating its deteriorative dispersion. And the decrease of specific surface area and pore volume for $Mn_{2/3}Co_8/Zr_{10}$-AC compared with Zr_{10}-AC could be interpreted.

3.3. *Surface chemical properties*

3.3.1. *Hydrogen temperature-programmed reduction*

H_2-TPR analysis was performed to evaluate the reducibility of active components and the activity of oxygen species on the Mn_xCo_y/Zr_z-AC with the total loading value of 8%. As shown in Fig. 8, two peaks with the maximum at around 605 and 715 °C were observed on Zr_8-AC, which was ascribed to the reduction of surface oxygen and the gasification of the AC support, respectively (Du et al., 2018a). It is worth mentioning that almost no reduction of ZrO_2 occurred below 900 °C according to previous researches (Zhao et al., 2018). With the dopant of cobalt oxides, two additional peaks assigned to the successive reduction of Co_3O_4 to CoO (at 328 °C) and CoO to metallic cobalt (at 434 °C) appeared (Bai and Li, 2014). And the peaks at 380 and 434 °C on Mn_1Co_4/Zr_4-AC were related to the reduction of MnO_2 or Mn_2O_3 to Mn_3O_4 and the further reduction to MnO (Todorova et al., 2010). Evidently, for both two samples, the reduction of surface oxygen and gasification of C shifted to lower temperature, further implying the existence of SMSI. Besides, with higher peak area and lower reduction temperature for reduction of surface oxygen, the surface adsorbed oxygen on Co_4/Zr_4-AC was more active than that on Mn_1Co_4/Zr_4-AC, which was consistent with the study of Piumetti et al. (Fig. 2) (Chen et al., 2018).

In the case of the Mn-Co co-doping sample $Mn_{2/3}Co_8$/AC, the curve was deconvoluted into five peaks. In addition to the reduction of surface oxygen and gasification of C, three other peaks were assumed as the reduction of Co_3O_4 (293 °C), the overlapping of the reduction of CoO to metallic cobalt and Mn^{4+} to Mn^{3+} (444 °C), and the reduction of Mn^{3+} to Mn^{2+} (498 °C). Interestingly, compared with Co_4/Zr_4-AC and Mn_1Co_4/Zr_4-AC, a slight shift of reduction peaks to higher temperature, especially for Mn species, was also observed for $Mn_{2/3}Co_8$/AC. As shown in Fig. S2, the intenser peaks of $Mn_{2/3}Co_8$/AC indicated its higher crystallinity than Mn_1Co_4/Zr_4-AC and Co_4/Zr_4-AC. In general, a smaller size and higher dispersion always contribute to a lower reduction temperature, thus a stronger reducibility (Zhu et al., 2013). Therefore, the formed bulk metal oxides on $Mn_{2/3}Co_8$/AC should be responsible for the higher reduction temperature. On one hand, higher loading content of Mn-Co oxides would facilitate the formation of agglomeration on $Mn_{2/3}Co_8$/AC. On the other hand, the addition of ZrO_2 gave rise to a higher dispersion of supported active components for Co_4/Zr_4-AC and Mn_1Co_4/Zr_4-AC (Figs. 6 and 7). For $Mn_{2/3}Co_4/Zr_4$-AC, all peaks shifted to lower reduction temperature to a larger extent, leading to its lowest reduction temperature among all measured samples. Besides, compared with Co_4/Zr_4-AC, the reduction peaks at 458 and 565 °C showed the tendency to overlap and gradually formed one peak, and Bai et al. ascribed the phenomenon to the activation of surface lattice oxygen (Bai and Li, 2014). In our study, the surface lattice oxygen of Mn_1Co_4/Zr_4-AC was more active than that of Co_4/Zr_4-AC, as shown in Fig. 2. Therefore, it was deduced that the incorporation of MnO_x on $Mn_{2/3}Co_4/Zr_4$-AC facilitated the activation of lattice oxygen. Moreover, the higher dispersion of Mn-Co species on Zr_4-AC might also conduce to it. As summarized in Table 1, Co_4/Zr_4-AC exhibited a higher active metal dispersion of 4.36% relative to Mn_1Co_4/Zr_4-AC, and the addition of CoO_x on MnO_x modified Zr-AC significantly enhanced the dispersion of active components on the surface of Zr-AC. Thereinto, $Mn_{2/3}Co_4/Zr_4$-AC

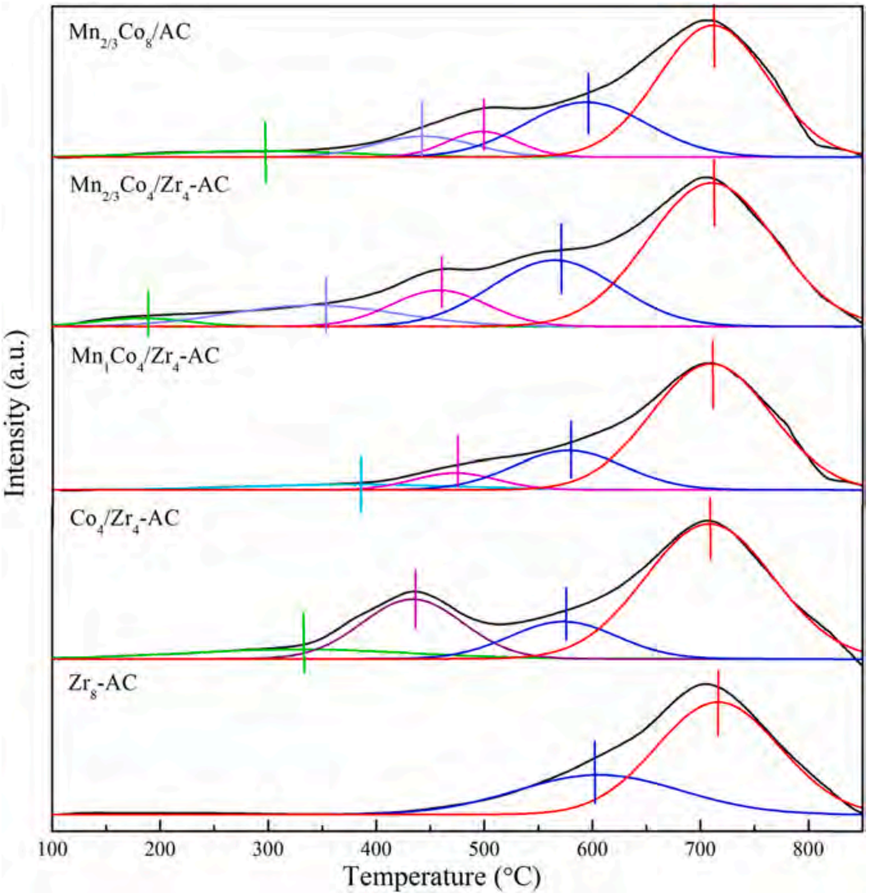

Fig. 8. H_2-TPR profiles of prepared samples.

possessed the highest dispersion of 6.67%, which verified the results of SEM. In conclusion, the highest reducibility of $Mn_{2/3}Co_4/Zr_4$-AC was mainly attributed to the following aspects: (i) the promotional effect of MnO_x on the mobility of lattice oxygen; (ii) the formation of surface oxygen with higher activity and the higher dispersion of MnO_x-CoO_x on Zr-AC with the aid of CoO_x; (iii) the further enhancement of the activity of lattice oxygen due to the higher dispersion of active components caused by ZrO_2.

3.3.2. X-ray photoelectron spectroscopy

To gain information on the atomic states and chemical composition of outermost layers of Mn_xCo_y/Zr_z-AC, XPS was carried out for the fresh samples. Fig. 9A showed the O1s XPS profiles of samples, in which three peaks were fitted. The peaks at around 530.2 eV, 531.2–531.7 eV and 532.2–532.4 eV were attributed to the lattice oxygen (O_L) that bonded with metal atoms in the form of O^{2-}, surface adsorbed oxygen, hydroxyl groups and oxygen vacancies (O_{OH}), and oxygen species in surface adsorbed water (O_W), respectively (Wang et al., 2017; Du et al., 2018a). In comparison of Co_4/Zr_4-AC, it was found that with the dopant of Mn, the binding energy of O 1 s decreased slightly, in which the electron-transfer from O to Mn or Co worked (Wang et al., 2009). Meanwhile, co-modified Zr_4-AC possessed a higher content of (O_L+O_{OH}), especially for O_{OH}. Thereinto, $Mn_{2/3}Co_4/Zr_4$-AC possessed the highest O_{OH} content of 53.87%, which was consistent with the activity tendency in HCHO and Hg^0 removal (Fig. 2). And with higher crystallinity, $Mn_{1/3}Co_4/Zr_4$-AC possessed a higher O_L than $Mn_{2/3}Co_4/Zr_4$-AC, as found by Tang et. al (2014). Moreover, with the same loading of MnO_x and CoO_x, the proportion of O_{OH} increased from 31.16% for $Mn_{2/3}Co_8$/AC to 66.92% for the sample supported on Zr_{10}-AC, revealing that Zr^{4+} contributed to accelerating the formation of O_{OH}. Similar results that Zr^{4+} doping facilitated the formation of surface –OH groups on catalysts was also reported by Huang et. al (2017). From the above, it could be deduced that both the synergy of Mn-Co oxides and the addition of ZrO_2 should be beneficial to the generation of more O_{OH}.

The XPS spectra of Mn $2p_{3/2}$ (Fig. 9B) were fitted into three peaks located at 641.1–641.2 eV, 642.5–642.8 eV and 644.5–644.9 eV, corresponding to Mn^{2+}, Mn^{3+} and Mn^{4+}, respectively (Fang et al., 2017). As shown in Table 2, Mn_1Co_4/Zr_4-AC owned the Mn^{4+}/Mn^{3+} ratio of 0.76, which was lower than the ratio of 0.84 calculated from H_2-TPR. The difference might be due to that the detection of XPS was just limited to the atoms on sample surface. Besides, Mn^{4+}/Mn^{3+} increased to 0.90 and 1.01 for $Mn_{2/3}Co_4/Zr_4$-AC and $Mn_{1/3}Co_4/Zr_4$-AC, respectively, whereas an elevated $(Mn^{4+}+Mn^{3+})/Mn^{2+}$ for the $Mn_{2/3}Co_4/Zr_4$-AC and a decreased one for $Mn_{1/3}Co_4/Zr_4$-AC was detected. It indicated that the acceleration on the formation of Mn atoms with higher valence varied with the molar ratio of Mn/Co. What's more, the promotion effect on Mn^{3+} and Mn^{4+} was also found for the modification of ZrO_2.

As shown in Fig. 9C, the species of Co^{3+} (780.2 ± 0.1 eV for Co $2p_{3/2}$ and 795.9 ± 0.1 eV for Co $2p_{1/2}$), Co^{2+} (782.1 ± 0.1 eV for Co $2p_{3/2}$ and 797.7 ± 0.1 eV for Co $2p_{1/2}$), along with the shake-up satellite peaks (787.6–787.7 eV and 803.4–805.5 eV) were detected on all prepared samples (Zhu et al., 2013). The incorporation of MnO_x led to an increase on the molar ratio of Co^{3+}/Co^{2+}, which rose from 0.39 for Co_4/Zr_4-AC to 0.82 and 0.63 for $Mn_{1/3}Co_4/Zr_4$-AC and $Mn_{2/3}Co_4/Zr_4$-AC, respectively. Following the electronic equilibrium, the lower Co^{3+}/Co^{2+} but higher $(Mn^{4+}+Mn^{3+})/Mn^{2+}$ of $Mn_{2/3}Co_4/Zr_4$-AC indicated the existence of redox cycle between MnO_x and CoO_x during the sample preparation. However, the inverse phenomenon was observed for the modification of ZrO_2, which promoted the generation of Co^{2+}. Fitting with its higher peak area of Co^{3+} reduction in H_2-TPR, $Mn_{2/3}Co_8$/AC possessed higher Co^{3+} content than $Mn_{2/3}Co_4/Zr_4$-AC. Besides, Co^{3+}/Co^{2+} decreased from 0.83 for $Mn_{2/3}Co_8$/AC to 0.44 for $Mn_{2/3}Co_8/Zr_{10}$-AC.

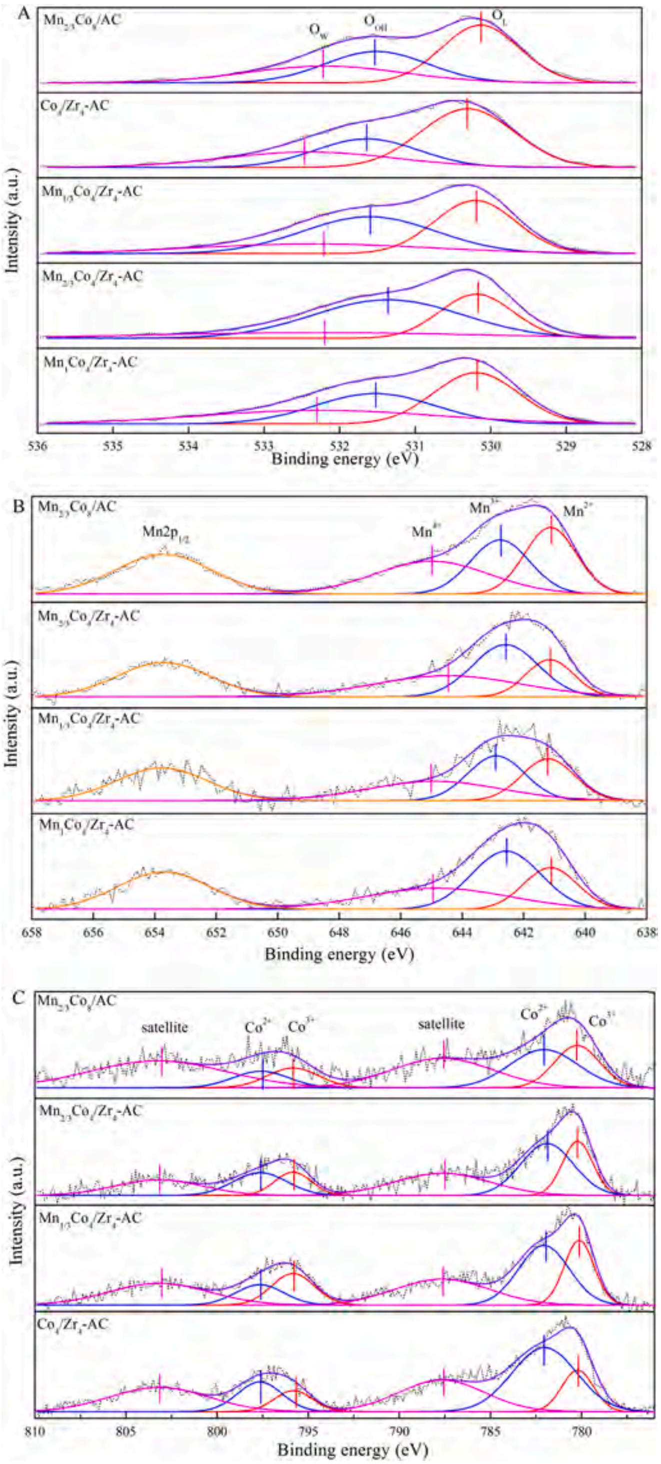

Fig. 9. XPS analysis of fresh Mn_xCo_4/Zr_4-AC and $Mn_{2/3}Co_8$/AC samples: (A) fitted O 1 s photoelectron peaks; (B) fitted Mn 2p photoelectron peaks; (C) fitted Co 2p photoelectron peaks.

4. Discussion

4.1. Physicochemical property-activity relationships

From the integrated characterizations discussed above, it was revealed that the modification of ZrO_2 on AC and the loading of Mn-Co mixed oxides on support affected many subsequent physico-chemical properties of Mn_xCo_y/Zr_z-AC, including the surface area, pore

Table 2
XPS relative intensity of fresh Mn_xCo_4/Zr_4-AC and $Mn_{2/3}Co_8$/AC samples.

Relative intensity	Mn_xCo_4/Zr_4-AC				$Mn_{2/3}Co_8$/AC
	x = 1	x = 2/3	x = 1/3	x = 0	
O_L (%)	38.88	30.23	37.67	49.71	43.61
O_{OH} (%)	32.44	53.87	42.81	26.58	31.16
O_W (%)	28.68	15.90	19.52	23.71	25.23
O_{OH}/O_L	0.83	1.78	1.14	0.53	0.72
[b]Mn^{2+} (%)	24.09	21.30	30.14	–	33.07
[b]Mn^{3+} (%)	43.21	41.44	34.82	–	30.74
[b]Mn^{4+} (%)	32.70	37.26	35.04	–	36.19
[b]Mn^{4+}/Mn^{3+}	0.76 ([c]0.84)	0.90	1.01	–	1.18
[b]$(Mn^{4+}+Mn^{3+})/Mn^{2+}$	3.15	3.70	2.32	–	2.02
Co^{2+} (%)	–	61.44	54.99	72.12	54.55
Co^{3+} (%)	–	38.56	45.01	27.88	45.45
Co^{3+}/Co^{2+}	–	0.63	0.82	0.39 ([c]0.42)	0.83
[d]Mn/Co (in mole)	–	1.94	0.46	–	1.82

[b] The XPS relative intensity and molar ratio of Mn atoms with difference valence in Mn $2p_{3/2}$.

[c] The molar ratio calculated by H_2-TPR.

[d] The molar ratio of Mn/Co measured by XPS.

structure, morphology, crystalline phase, valence state, reducibility and so on. As the key factors for the activity of samples, it is necessary to anatomize the effect of respective element on the simultaneous removal of HCHO and Hg^0.

As displayed in Table 1 and Fig. 6, there existed some essentially structural and morphological differences between the samples with Zr-AC support and the samples with AC support. Compared with virgin AC, a higher surface area and larger pore volume, due to the generation of narrow channels, was observed on Zr-AC. And higher surface area of Zr-AC support contributed to the subsequent dispersion of Mn-Co oxides on its surface, as testified by that the molar ratio of Mn/Co on $Mn_{2/3}Co_8/Zr_{10}$-AC surface measured by XPS was closer to the nominal value than that of $Mn_{2/3}Co_8$/AC (Tables 2 and 3). Moreover, the ZrO_2 doping on AC further led to a higher dispersion of Mn-Co oxides compared with that on Mn_xCo_y/AC, and thus a lower crystallinity detected by XRD.

Analogously, Mn_xCo_y/Zr-AC also possessed many structural and morphological distinctions with each other, mainly due to the molar ratio of Mn/(Mn+Co) and the loading value of Mn-Co oxides. With the loading of 4% Mn-Co oxides, an increase of BET surface area and pore volume was observed, while it was inverse for the doping of 8% Mn-Co oxides on account of the formed agglomeration. Besides, the cooperation of MnO_x and CoO_x also endowed the sample with a higher BET surface area for Mn_xCo_4/Zr_4-AC. In general, larger surface area and pore volume can always provide more adsorption sites to be in favor of the adsorption of gas reactants, as well as the mobility of gas-phase oxygen and surface active oxygen in samples, thus a superior activity (Xu et al., 2015b). However, it is not always the case here. Although with a lower surface area and pore volume than $Mn_{1/3}Co_4/Zr_4$-AC, both the highest dispersion and smallest nano-particles were obtained for $Mn_{2/3}Co_4/Zr_4$-AC, and the highest HCHO and Hg^0 removal efficiency were also reached. Overall, the structure and morphology could not be the decisive factor determining the activity of Mn_xCo_y/Zr_z-AC.

Table 3
XPS relative intensity of fresh and used $Mn_{2/3}Co_8/Zr_{10}$-AC treated with HCHO + Hg^0, HCHO and Hg^0, respectively.

Relative intensity	Fresh sample	Used sample		
		HCHO + Hg^0	HCHO	Hg^0
O_L (%)	21.30	25.17	28.74	22.71
O_{OH} (%)	66.92	50.82	44.50	52.82
O_W (%)	11.78	24.01	26.76	24.47
[b]Mn^{2+} (%)	24.23	23.74	29.77	27.58
[b]Mn^{3+} (%)	37.29	48.25	44.53	46.31
[b]Mn^{4+} (%)	38.48	28.01	25.70	26.11
Co^{2+} (%)	69.05	57.35	45.33	55.75
Co^{3+} (%)	30.95	42.65	54.67	44.25
Co^{3+}/Co^{2+}	0.45	0.74	0.83	0.79
Hg $4f_{7/2}$ (%)	–	–	–	12.66
Si 2p (%)	–	80.90	–	58.97
Hg $4f_{5/2}$ (%)	–	19.10	–	28.37
[d]Mn/Co (in mole)	2.02			

[b] The XPS relative intensity and molar ratio of Mn atoms with difference valence in Mn $2p_{3/2}$.

[d] The molar ratio of Mn/Co measured by XPS.

As depicted in Fig. 4, the HCHO removal on $Mn_{2/3}Co_8/Zr_{10}$-AC mainly proceeded as oxidation, accompanied with a small portion of adsorption which decreased with elevated temperature. Differently, adsorption was proved to predominate in Hg^0 elimination on $Mn_{2/3}Co_8/Zr_{10}$-AC through the mercury speciation conversion test, and only lower than 24.83% of mercury oxidation was detected. As known to all, structural property is decisive to the physisorption of reactants, while the chemisorption behavior is mainly dependent on the surface active oxygens species and active sites (Zeng et al., 2017). To further determine the adsorptive behavior of Hg^0 on sample, Hg-TPD was carried out (Fig. S3). The Hg-TPD profile was divided into three regions, corresponding to weakly adsorbed HgO (318 °C), strong bonded HgO (384 °C) and O_L-HgO (469 °C), whereas no peak relevant to the physical adsorption of Hg^0 was observed (Liu et al., 2019). Obviously, Hg^0 removal over Mn_xCo_y/Zr_z-AC was mainly in the form of chemisorption, in which the surface active oxygen and active sites is crucial. The diverse mechanism of HCHO and Hg^0 removal could account for their different tendency varied with reaction temperature, in which physisorption is an exothermal process while chemisorption and oxidation is endothermal reaction (Zeng et al., 2017). Therefore, the surface chemical property was of significant importance for the activity of Mn_xCo_y/Zr_z-AC in terms of the simultaneous removal of HCHO and Hg^0.

According to H_2-TPR (Fig. 8), with lower reduction temperature and larger peak area, $Mn_{2/3}Co_4/Zr_4$-AC exhibited the higher reducibility (Li et al., 2016). In combination with above studies, the formed lattice oxygen with high mobility and surface oxygen with high activity via the synergy between MnO_x and CoO_x, the higher dispersion and smaller particle size with the aid of ZrO_2 should be mainly responsible for it. The high reducibility of sample was reported to conduce to its excellent activity (Liang et al., 2016). On one hand, the enhanced reducibility would promote the active oxygen to transfer on the gas-solid interface, and thus facilitate the combination of active oxygen and adsorbed reactants during the simultaneous removal of HCHO and Hg^0. On the other hand, lattice oxygen with high mobility made it easier for gas-phase oxygen to migrate between surface lattice oxygen and oxygen vacancies, which was conductive to the formation of surface active oxygen species, and has been proved to give an important contribution to the oxidation activity of samples (Zhu et al., 2017).

In addition to redox capability, the activity of sample was also closely connected with the atomic valence states of surface active components. As demonstrated by XPS results, both the ZrO_2 addition and co-modification of Mn-Co oxides promoted the formation of both O_L and O_{OH}, especially for O_{OH}. The relationship between the O_{OH}/O_L of Mn_xCo_y/Zr_z-AC and the catalytic activity of samples for HCHO was summarized in Fig. S4. With the highest O_{OH}/O_L, $Mn_{2/3}Co_8/Zr_{10}$-AC exhibited the lowest T_{10} and T_{50}, as well as T_{90} of 209 °C, which was even lower than the T_{50} of Mn_1Co_4/Zr_4-AC and Co_4/Zr_4-AC. Higher O_{OH}/O_L the sample possessed, lower T_{10} and T_{50} were, and higher activity the sample exhibited. The positive correlation between the activity of sample and O_{OH}/O_L was also found for Hg^0 removal on Mn_xCo_4/Zr_4-AC. Therefore, the higher O_{OH} concentration could promote both adsorption and oxidation of HCHO and Hg^0, and thus endowed the sample with higher catalytic activity (Wu et al., 2015; Wang et al., 2017). High O_{OH} concentration generated on $Mn_{2/3}Co_4/Zr_4$-AC might be contributed to the following two aspects. One was that Mn^{4+} and Co^{3+}, as the direct oxidizer participated in HCHO and Hg^0 removal, could produce more surface adsorbed oxygen species. The other was the existence of metal atoms with lower valences, such as Mn^{3+}, Mn^{2+} and Co^{2+}. It is well-known that once the reduced metal oxides appear, oxygen vacancies will be generated to maintain electrostatic balance according to the following process (Fang et al., 2018):

$$\begin{aligned} &4Mn^{4+}/Mn^{3+} + O^{2-} \rightarrow 4Mn^{4+}/Mn^{3+} + 2e^-/V_o + 1/2O_2 \\ &\rightarrow 2Mn^{4+}/Mn^{3+} + 2Mn^{3+}/Mn^{2+} + V_o + 1/2O_2 \end{aligned} \tag{8}$$

$$4Co^{3+} + O^{2-} \rightarrow 4Co^{3+} + 2e^-/V_o + 1/2O_2 \rightarrow 2Co^{3+} + 2Co^{2+} + V_o + 1/2O_2 \tag{9}$$

where V_o presents an oxygen vacancy. When at the existence of molecular oxygen and water vapor, the dissociation of H_2O into hydroxyl groups by oxygen vacancy, as well as the generation of active oxygen species via the occupation of V_o by gaseous oxygen with a lower chemical adsorption energy, tend to participate in the interaction between catalyst surface and reactant (Fang et al., 2018; He et al., 2019b). Besides, the presence of V_o also could enhance the mobility of lattice oxygen (Huang et al., 2017). It is worth noting that the sample with higher Co^{2+} rather than Co^{3+}, such as $Mn_{2/3}Co_4/Zr_4$-AC and $Mn_{2/3}Co_8/Zr_{10}$-AC, exhibited higher activity, which was not consistent with previous studies (Zhu et al., 2013; Bai and Li, 2014). In this sense, the promotion of Co^{2+} on the generation of oxygen vacancy should be responsible for it. Moreover, the storage and release of surface active oxygen species through the redox cycle $Mn^{4+}/Mn^{3+} + Co^{2+} \leftrightarrow Mn^{3+}/Mn^{2+} + Co^{3+}$, as testified by XRD and XPS, was also beneficial for the superior activity of Mn_xCo_y/Zr_z-AC as the continuous provider of active oxygen species for the oxidation of adsorbed HCHO and Hg^0.

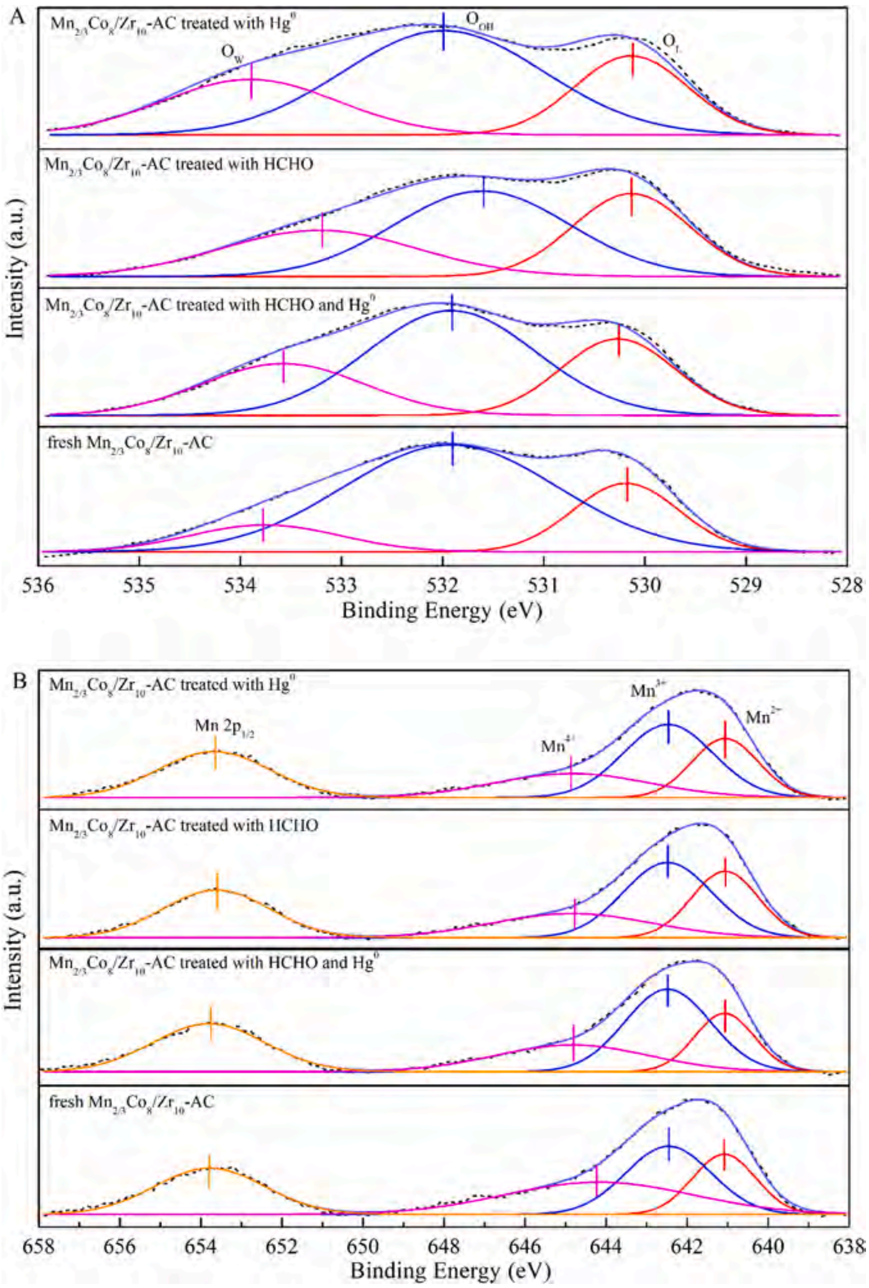

Fig. 10. XPS analysis of fresh and treated $Mn_{2/3}Co_8/Zr_{10}$-AC: (A) fitted O 1 s photoelectron peaks; (B) fitted Mn 2p photoelectron peaks; (C) fitted Co 2p photoelectron peaks; (D) fitted Hg 4f photoelectron peaks.,.

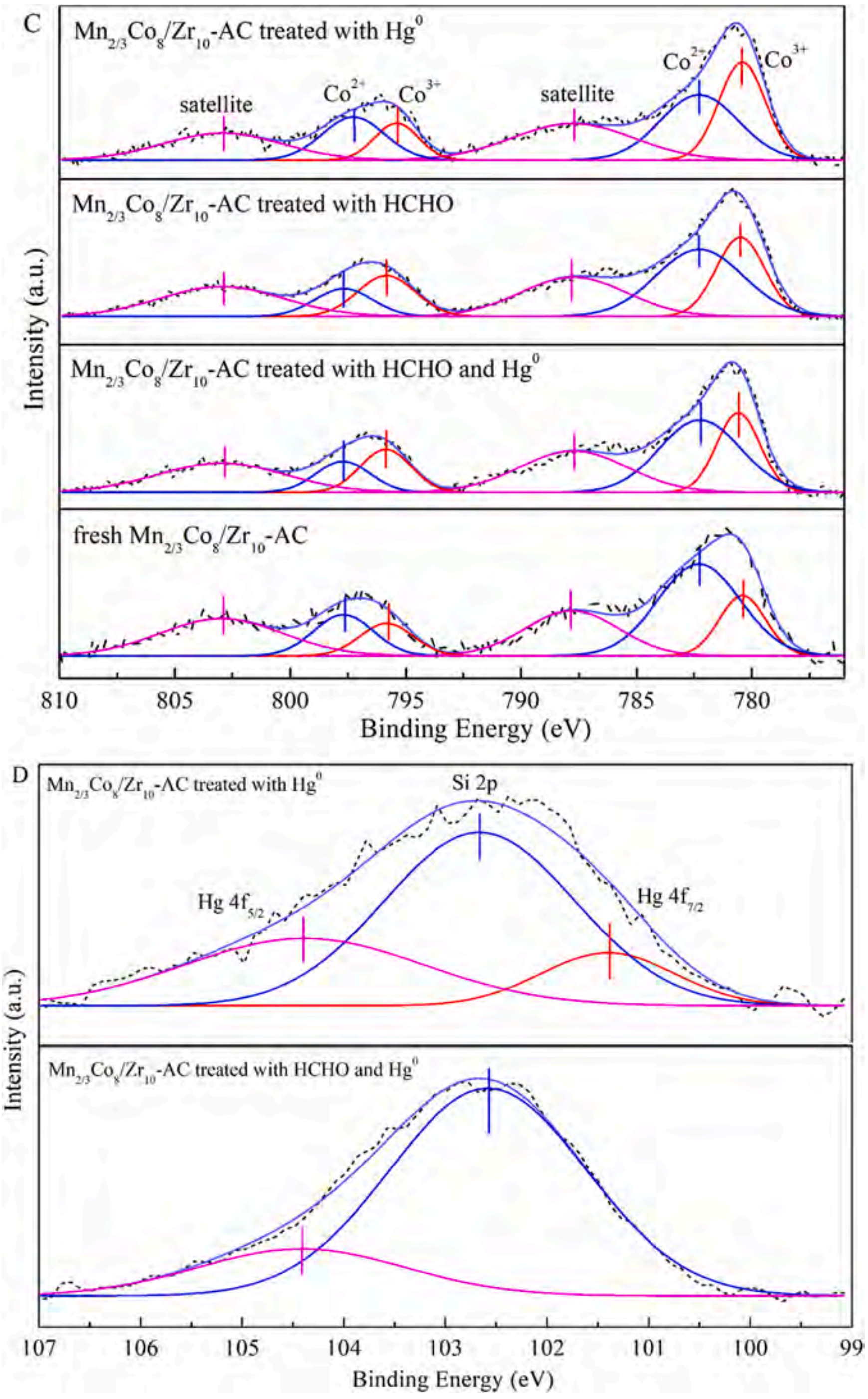

Fig. 10. (*continued*).

4.2. *Proposed mechanism*

To explore the change of the surface components during HCHO and Hg^0 removal on $Mn_{2/3}Co_8/Zr_{10}$-AC, XPS was conducted for fresh and treated samples, as shown in Fig. 10 and Table 3. In comparison with fresh $Mn_{2/3}Co_8/Zr_{10}$-AC sample, a sharp increase of O_W, as well as a rapid decrease of O_{OH}, was observed for all three treated samples, implying the consumption of surface active oxygen and the formation of adsorbed water during the reaction. Remarkably, the content of lattice oxygen increased slightly, rather than decreased as reported in previous studies, whether the sample was treated with HCHO and/or Hg^0 (Chen et al., 2018; Yi et al., 2018). Besides, the lowest O_{OH} and O_L was detected on $Mn_{2/3}Co_8/Zr_{10}$-AC treated with HCHO and $Mn_{2/3}Co_8/Zr_{10}$-AC treated with Hg^0 alone, respectively. It could be concluded that the adsorbed HCHO was oxidized by O_{OH} preferentially, and more lattice oxygen participated in Hg^0 removal. In terms of Mn species, the tendency of decreased $(Mn^{4+}+Mn^{3+})/Mn^{2+}$ was observed for $Mn_{2/3}Co_8/Zr_4$-AC treated with HCHO or Hg^0, while the sample treated with HCHO + Hg^0 possessed an increased $(Mn^{4+}+Mn^{3+})/Mn^{2+}$, but decreased Mn^{4+} content. It indicated that Mn atoms with higher valence, especially for Mn^{4+}, was reduced, and provided active oxygen for the removal of HCHO and/or Hg^0. On the contrary, the ratio of Co^{3+}/Co^{2+} increased after treatment, which in turn accounted for the increase of O_L (Fig. 10A). It could be concluded that the redox cycle $Mn^{4+}/Mn^{3+} + Co^{2+} \leftrightarrow Mn^{3+}/Mn^{2+} + Co^{3+}$ occurred as a provider of active oxygen, through storing and releasing oxygen atoms, for the simultaneous removal of HCHO and Hg^0.

Hg 4f XPS spectra of $Mn_{2/3}Co_8/Zr_{10}$-AC treated with Hg^0 were examined to identify the species of adsorbed mercury. As displayed in Fig. 10D, apart from the peak corresponding to Si 2p at 102.6 eV, two peaks relevant to Hg 4f were fitted for $Mn_{2/3}Co_8/Zr_{10}$-AC treated with Hg^0 (He et al., 2020). Obvious peaks at 101.4 eV and 104.3 eV were ascribed to Hg $4f_{7/2}$ and Hg $4f_{5/2}$, respectively, demonstrating HgO as the main mercury species adsorbed on the sample surface (Zhang et al., 2017). And consistent with Hg-TPD, the peak associated with Hg^0 at ~99.9 eV was absent. The desorption of adsorbed Hg^0 from the sample surface or its low concentration below the detection limit of XPS measurement should be responsible for it. After simultaneous removal of HCHO and Hg^0, the peak relevant to HgO was only detected at 104.3 eV with a lower relative intensity of 19.10%, indicating the weakened adsorption of Hg^0 as shown in Fig. 5. To further identify how HCHO affect the Hg^0 removal, Hg-TPD was also conducted for $Mn_{2/3}Co_8/Zr_{10}$-AC treated with Hg^0 (Fig. S3). Without HCHO, all three peaks, with the sharply increased peak area, shifted to a lower desorption temperature. Generally speaking, lower temperature the desorption peak appeared at, weaker interaction forces between the mercury and adsorption sites were, and easier the adsorption of mercury on active sites were (Xu et al., 2015a). Notably, the absence of HCHO led to a sharp increase for the proportion of HgO bonded with O_L, which increased from 14.13% to 30.18%. The least increase of O_L over $Mn_{2/3}Co_8/Zr_{10}$-AC treated with Hg^0 also confirmed the phenomenon. And a lower proportion of 15.19% and 0.86% was observed for strongly-bonded HgO and weakly-adsorbed HgO on $Mn_{2/3}Co_8/Zr_{10}$-AC treated with Hg^0, respectively. It indicated that the HCHO gave preference to competing the lattice oxygen with Hg^0, followed by the chemisorbed oxygen.

To give a further analysis on the removal process of HCHO, the in-situ DRIFTS spectra of $Mn_{2/3}Co_8/Zr_{10}$-AC obtained in a flow of HCHO + O_2 + H_2O/N_2 at 240ºC were shown in Fig. 11. Upon exposure to 120 ppm HCHO + 6% O_2 + 8 vol% H_2O/N_2, the peaks ascribed to molecularly adsorbed HCHO appeared at 1015 cm^{-1} (Huang et al., 2013a). With prolongation of reaction time, the intensity of peaks increased initially and then a slight decrease was observed after 30 min. The bands at 2900, 1058 and 805 cm^{-1} were assigned to $\nu_s(CH_2)$, $\omega(CH_2)$ and ν(C-O) of dioxymethylene (DOM), respectively (Raskó et al., 2004; Lochař, 2006; Ma and Zhang, 2016). It could be inferred that HCHO was molecularly adsorbed on the sample surface at first, and followed by its quick oxidation into DOM through the combination of electrophilic carbon of the carbonyl group with the nucleophilic surface oxygen, as reported by previous researches (Lochař, 2006; He and Ji, 2010). And the dynamic equilibrium between the formation and further oxidation of DOM was reached after 40 min. When the reaction proceeded for 5 min, the formate species, derived from DOM oxidized by active oxygen on the sample surface, was also found. The slight adsorption bands at 1620 and 1380 cm^{-1} were associated with the $\nu_{as}(COO)$ and $\nu_s(COO)$ of formate species, respectively (Xu et al., 2015a). As reported (Durand et al., 2010), formate species could be adsorbed on the sample surface through bidentate (chelating), bridging and monodentate configuration, which could be distinguished by the frequency separation between $\nu_{as}(COO)$ and $\nu_s(COO)$. In this work, the frequency separation of 240 cm^{-1} manifested the formate species was bonded to the sample in a bridging configuration (Barros et al., 2005). The increased intensity of bands relevant to formate species demonstrated the accelerated oxidation of DOM, as well as the accumulation of formate species, on sample surface until reach the equilibrium after reacted for 30 min. It is worth noting that the equilibrium between the formation and further oxidation of formate species was reached more quickly than that of DOM. Moreover, the peaks at 3478 cm^{-1} and 2330–2350 cm^{-1} revealed the further oxidation of formate species to H_2O and CO_2 (Busca et al., 1987; Chen et al., 2013). The adsorbed CO_2 was observed when reacted 5 min, and up to the maximum at 40 min. And the following decrease with progress of reaction might be attributed to the desorption of CO_2 from the sample to some extent, which was consistent with the CO_2 detected in outlet gas (Fig. 4). The consumption of surface hydroxyl (-OH) was also observed as the negative band at 3700 cm^{-1}, which was continuously supplemented via the activation of adsorbed H_2O molecules by active oxygen species (Busca et al., 1987). The peaks relevant to the formation of a metal-oxo band between carboxylic group (COO–) and Mn or Co ions at 685 cm^{-1} demonstrated the MnO_x and CoO_x could act as the active sites for HCHO removal (Bahri et al., 2017). In combination with the formed species occurred during HCHO removal, it could be concluded that the oxidation of

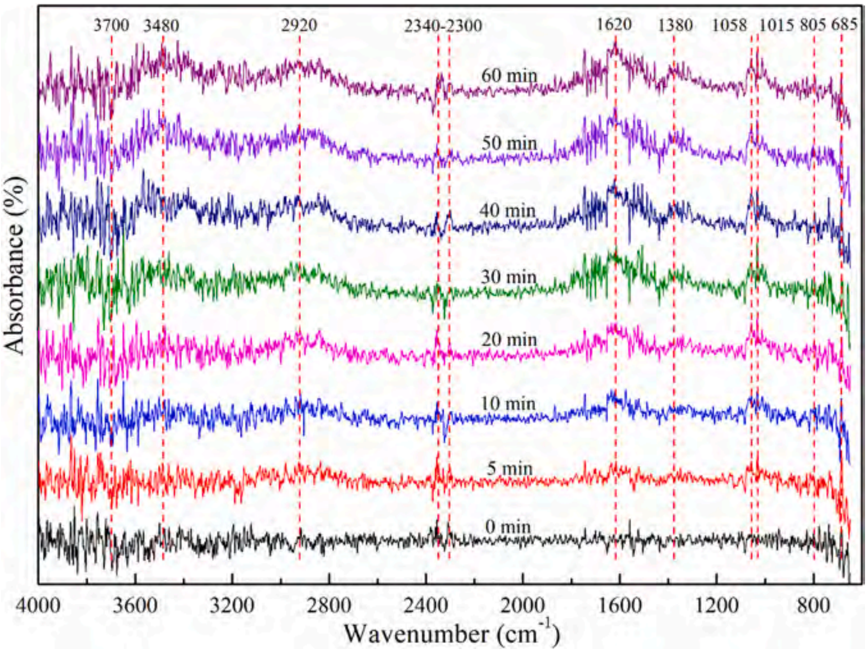

Fig. 11. Dynamic changes of in situ DRIFTS for the $Mn_{2/3}Co_8/Zr_{10}$-AC sample as a function of reaction time in a flow of 120 ppm HCHO + 6% O_2 + 8 vol% H_2O/N_2 at 240 °C.

intermediates, especially the oxidation of DOM into formate species, was the rate-limiting step during the whole catalytic oxidation of HCHO. And the accumulation of intermediates would occupy the active sites, and thus caused the deactivation of sample. In-depth study concerning how to accelerate the oxidation of intermediates will be conducted in our future study.

Based on above discussion, the mechanism of simultaneous removal of HCHO and Hg^0 on Mn_xCo_y/Zr_z-AC was proposed. In previous studies (Piumetti et al., 2015; Liu et al., 2016), VOCs removal on metal oxides-supported sample followed a Mars–Van Krevelen (MVK) mechanism, in which VOCs molecules reacted with active oxygen on different redox sites over sample surface. During the process, the oxidation of VOC molecules by the active oxygen of the sample, that is the reduction of samples, and then the re-oxidation of sample through the supplement of active oxygen by gas-phase oxygen and water vapor were involved. As shown in Fig. 12, HCHO was molecularly adsorbed on sample surface through the active sites, including O_{OH} and active oxygen in Mn-Co oxides at first. Then the adsorbed HCHO was oxidized into DOM through active oxygen species (O*) attracting carbonyl group of adsorbed HCHO, and followed by the further oxidation of DOM into formate species, which bonded to the sample in a bridging configuration. Finally, the formate species was oxidized into CO_2 and H_2O, and desorbed from sample. During the reaction, the redox cycle between Mn and Co proceeded and provided continuous O*, and the consumed active oxygen species were supplemented by the gaseous O_2 and H_2O. In terms of Hg^0 removal, the adsorbed Hg^0 was oxidized into HgO through bonding with O*, and a spot of HgO desorbed from sample. Moreover, the adsorbed HCHO was oxidized by O_{OH} preferentially, while more lattice oxygen participated in Hg^0 removal. In aforementioned pathway, porous structure with higher surface area and larger pore size, well-dispersed Mn-Co oxides, higher reducibility, higher content of Mn atoms with higher valence and Co^{2+}, and abundant active oxygen species, including lattice oxygen with higher mobility, more surface adsorbed oxygen and hydroxyl groups, as well as oxygen vacancies that could be filled by gas-phase oxygen and water vapor to form active surface oxygen, conduced to the superior activity of $Mn_{2/3}Co_8/Zr_{10}$-AC for the simultaneous removal of HCHO and Hg^0.

5. Regeneration performance

As a critical criterion for practical application, the stability of sample was evaluated through recycle experiment of $Mn_{2/3}Co_8/Zr_{10}$-AC. As found in Fig. 13A, decreasing outlet concentration of HCHO was observed in the initial regeneration cycles as compared to that obtained for fresh sample, and the highest activity was reached for the sample regenerated after three recycle. Then a slight decrease of 4.40% and 4.63% in HCHO removal efficiency occurred in the following 4th cycle and 5th cycle, respectively. Differing from HCHO removal, a moderate deactivation with a decrease in Hg^0 removal from 82.56% to 72.97% was detected after five recycle. Probably the collapse of some micropores during the regeneration should be responsible for the observed decrease in activity, especially for Hg^0 adsorption. Additionally, the irreversible occupancy of some active sites also contributed to the deactivation. It was manifested that the sample $Mn_{2/3}Co_8/Zr_{10}$-AC exhibited an excellent activity and stability in the simultaneous removal of HCHO and Hg^0.

6. Conclusion

The performance of Mn_xCo_y/Zr_z-AC was evaluated for simultaneous removal of HCHO and Hg^0. The optimal $Mn_{2/3}Co_8/Zr_{10}$-AC exhibited enhanced activity for the simultaneous removal of HCHO and Hg^0 with 99.87% HCHO removal efficiency and 82.41% Hg^0 removal efficiency at 240°C, and superior stability through the recycle experiment. The mechanism on promotional removal of HCHO and Hg^0 over Mn_xCo_y/Zr_z-AC was systematically investigated by N_2 adsorption-desorption, SEM, XRD, H_2-TPR, H_2 pulse chemisorption, XPS, Hg-TPD and in-situ DRIFTS. As an effective support, Zr-AC possessed a higher surface area and pore volume, and conduced to the highly-dispersed active components and a higher reducibility, which was further strengthened by the following modification of Mn-Co oxides. Besides, the co-dopant of Mn-Co oxides not only led to lattice oxygen with high mobility, abundant surface adsorbed oxygen species, Mn atoms with higher valence, and a higher O_{OH}/O_L, but also constituted the redox cycle $Mn^{4+}/Mn^{3+} + Co^{2+} \leftrightarrow Mn^{3+}/Mn^{2+} + Co^{3+}$ as the provider of active oxygen for simultaneous removal of HCHO and Hg^0. XPS and Hg-TPD indicated that Hg^0 removal mainly proceeded as the combination of chemisorption, occupying the dominant position, and oxidation. In-situ

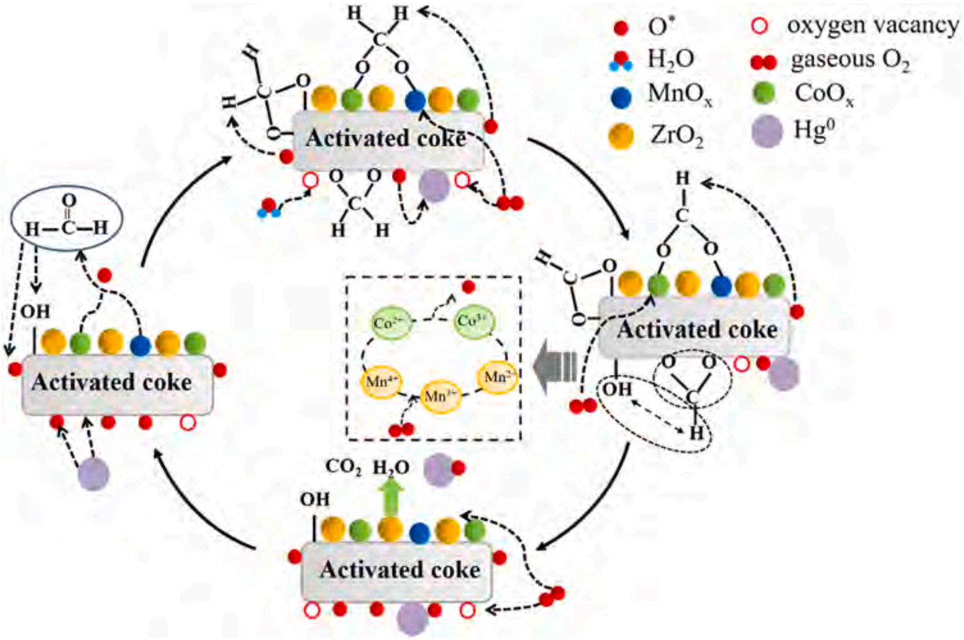

Fig. 12. The proposed mechanism on the simultaneous removal of HCHO and Hg^0 over Mn_xCo_y/Zr_z-AC.

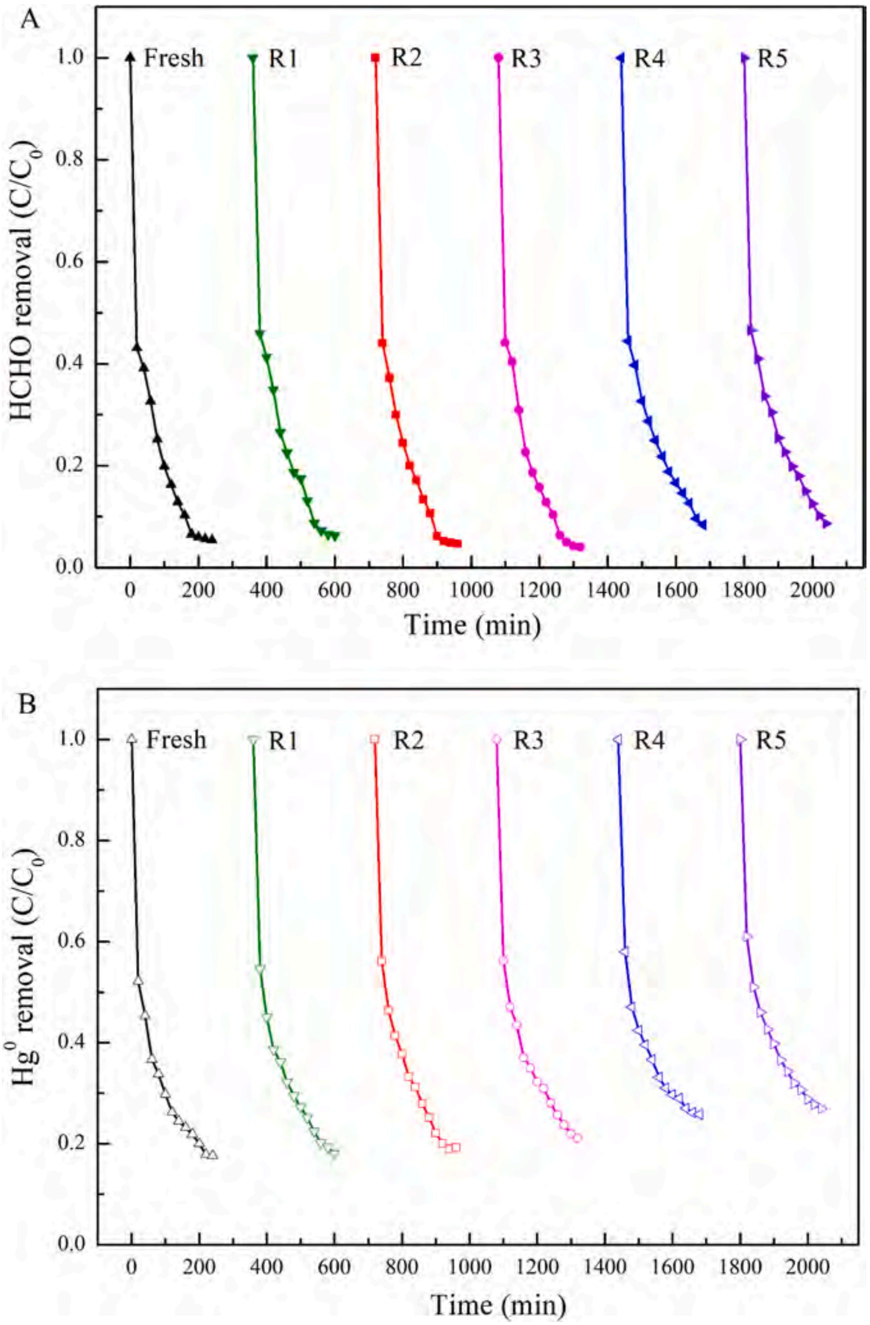

Fig. 13. Recycle performance of $Mn_{2/3}Co_8/Zr_{10}$-AC towards the simultaneous removal of (A) HCHO and (B) Hg^0. (Reaction condition: 120 ppm HCHO, 100 μg/m^3 Hg^0, 6% O_2, 8 vol% H_2O, total flow rate 500 mL/min, 10 g sample, reaction temperature 240 °C).

DRIFTS proved that the DOM and formate intermediates were formed and then were oxidized into CO_2 and H_2O. Moreover, HCHO gave preference to competing the lattice oxygen with Hg^0, and thus suppressed the Hg^0 removal. The work might provide some scientific guidance for developing efficient AC-based catalysts for the simultaneous control of HCHO and Hg^0.

CRediT authorship contribution statement

Xueyu Du: Conceptualization, Methodology, Investigation, Writing - original draft, Data curation, Validation. **Caiting Li:** Conceptualization, Supervision, Writing - review & editing, Funding acquisition. **Jie Zhang:** Methodology, Writing - review & editing. **Lingkui Zhao:** Writing - review & editing. **Shanhong Li:** Supervision. **Yue Lyu:** Writing - review & editing. **Yindi Zhang:** Writing - review & editing. **Youcai Zhu:** Writing - review & editing. **Le Huang**: Conceptualization.

Declaration of Competing Interest

The authors declare that they have no known competing financial interests or personal relationships that could have appeared to influence the work reported in this paper.

Acknowledgment

This work was financially supported by the National Key Research and Development Program of China (2016YFC0204100) and the Key Research and Development Program of Hunan Province in China (2018SK2032).

Appendix A. Supporting information

Supplementary data associated with this article can be found in the online version at doi:10.1016/j.jhazmat.2020.124830.

References

Agrell, J., Birgersson, H., Boutonnet, M., Cabrera, I.M., Navarro, R.M., Fierro, J.L.G., 2003. Production of hydrogen from methanol over Cu/ZnO catalysts promoted by ZrO_2 and Al_2O_3. J. Catal. 219, 389–403.

An, J.T., Shang, K.F., Lu, N., Jiang, Y.Z., Wang, T.C., Li, J., Wu, Y., 2014. Performance evaluation of non-thermal plasma injection for elemental mercury oxidation in a simulated flue gas. J. Hazard. Mater. 268, 237–245.

Bahri, M., Haghighat, F., Rohani, S., Kazemian, H., 2017. Metal organic frameworks for gas-phase VOCs removal in a NTP-catalytic reactor. Chem. Eng. J. 320, 308–318.

Bai, B.Y., Li, J.H., 2014. Positive effects of K^+ ions on three-dimensional mesoporous Ag/Co_3O_4 catalyst for HCHO oxidation. ACS Catal. 4, 2753–2762.

Barros, R.B., Garcia, A.R., Ilharco, L.M., 2005. The chemistry of formic acid on oxygen modified Ru (001) surfaces. Surf. Sci. 591, 142–152.

Busca, G., Lamotte, J., Lavalley, J.C., Lorezelli, V., 1987. FT-IR study of the adsorption and transformation of formaldehyde on oxide surfaces. J. Am. Chem. Soc. 109, 5197–5202.

Chen, S.S., Hsi, H.C., Nian, S.H., Chiu, C.H., 2014. Synthesis of N-doped TiO_2 photocatalyst for low-concentration elemental mercury removal under various gas conditions. Appl. Catal. B: Environ. 160–161, 558–565.

Chen, J., Jiang, M.Z., Xu, W.J., Chen, J., Hong, Z.X., Jia, H.P., 2019. Incorporating Mn cation as anchor to atomically disperse Pt on TiO_2 for low-temperature removal of formaldehyde. Appl. Catal. B: Environ. 259, 118013.

Chen, J.Q., Li, C.T., Li, S.H., Lu, P., Gao, L., Du, X.Y., Yi, Y.Y., 2018. Simultaneous removal of HCHO and elemental mercury from flue gas over Co-Ce oxides supported activated coke impregnated by sulfuric acid. Chem. Eng. J. 338, 358–368.

Chen, B.B., Shi, C., Crocker, M., Wang, Y., Zhu, A.M., 2013. Catalytic removal of formaldehyde at room temperature over supported gold catalysts. Appl. Catal. B: Environ. 132 133, 245–255.

Chi, G.L., Shen, B.X., Yu, R.R., He, C., Zhang, X., 2017. Simultaneous removal of NO and Hg^0 over Ce-Cu modified V_2O_5/TiO_2 based commerical SCR catalysts. J. Hazard. Mater. 330, 83–92.

Durand, J.P., Senanayake, S.D., Suib, S.L., Mullins, D.R., 2010. Reaction of formic acid amorphous manganese oxide catalytic systems: an in situ study. J. Phys. Chem. C. 114, 20000–20006.

Du, X.Y., Li, C.T., Zhao, L.K., Zhang, J., Gao, L., Sheng, J.J., Yi, Y.Y., Chen, J.Q., Zeng, G. M., 2018. Promotional removal of HCHO from simulated flue gas over Mn-Fe oxides modified activated coke. Appl. Catal. B: Environ. 232, 37–48.

Du, J.P., Qu, Z.P., Dong, C., Song, L.X., Qin, Y., Huang, N., 2018. Low-temperature abatement of toluene over Mn-Ce oxides catalysts synthesized by a modified hydrothermal approach. Appl. Surf. Sci. 433, 1025–1035.

Fang, N.J., Guo, J.X., Shu, S., Li, J.J., Chu, Y.H., 2017. Influence of textures, oxygen-containing functional groups and metal species on SO2 and NO removal over Ce-Mn/NAC. Fuel 202, 328–337.

Fang, R.M., Huang, H.B., Ji, J., He, M., Feng, Q.Y., Zhan, Y.J., Leung, D.Y.C., 2018. Efficient MnOx supported on coconut shell activated carbon for catalytic oxidation of indoor formaldehyde at room temperature. Chem. Eng. J. 334, 2050–2057.

Finocchio, E., Busca, G., 2001. Characterization and hydrocarbon oxidation activity of coprecipitated mixed oxides Mn3O4/Al2O3. Catal. Today 70, 213–225.

Garcia, J.P., Beyne-Masclet, S., Mouvier, G., Masclet, P., 1992. Emissions of volatile organic compounds by coal-fired power stations. Atmos. Environ. 26, 1589–1597.

Gelles, T., Keishnamurthy, A., Adebayo, B., Rownaghi, A., Rezaei, F., 2020. Abatement of gaseous volatile organic compounds: a material perspective. Catal. Today 350, 3–18.

He, C., Cheng, J., Zhang, X., Douthwaite, M., Pattisson, S., Hao, Z.P., 2019. Recent advances in the catalytic oxidation of volatile organic compounds: a review based on pollutant sorts and sources. Chem. Rev. 119, 4471–4568.

He, Y.B., Ji, H.B., 2010. In-situ DRIFTS study on catalytic oxidation of formaldehyde over Pt/TiO2 under mild conditions. Chin. J. Catal. 31, 171–175.

He, M., Ji, J., Liu, B.Y., Huang, H.B., 2019. Reduced TiO_2 with tunable oxygen vacancies for catalytic oxidation of formaldehyde at room temperature. Appl. Surf. Sci. 473, 934–942.

He, J., Lai, C., Qin, L., Li, B., liu, S., Jiao, L., Fu, Y., Huang, D., Li, L., Zhang, M., Liu, X., Yi, H., Chen, L., Li, Z., 2020. Strategy to improve gold nanoparticles loading efficiency on defect-free high silica ZSM-5 zeolite for the reduction of nitrophenols. Chemosphere 256, 127083.

Huang, C., Ding, Y.P., Chen, Y.W., Li, P.W., Zhu, S.M., Shen, S.B., 2017. Highly efficient Zr doped-TiO_2/glass fiber photocatalyst and its performance in formaldehyde removal under visible light. J. Environ. Sci. 60, 61–69.

Huang, K.J., Kong, L.C., Yuan, F.L., Xie, C.S., 2013. In situ diffuse reflectance infrared Fourier transform spectroscopy study of formaldehyde adsorption and reactions on nano γ-Fe_2O_3 films. Appl. Surf. Sci. 270, 405–410.

Huang, Q., Ma, W.J., Yan, X.K., Chen, Y.W., Zhu, S.M., Shen, S.B., 2013. Photocatalytic decomposition of gaseous HCHO by $Zr_xTi_{1-x}O_2$ catalysts under UV–vis light irradiation with an energy-saving lamp. J. Mol. Catal. A: Chem. 366, 261–265.

Jiang, H.X., Niu, Y., Wang, Q.Y., Chen, Y.F., Zhang, M.H., 2018. Single-phase SO_2-resistant to poisoning Co/Mn-MOF-74 catalysts for NH_3-SCR. Catal. Commun. 113, 46–50.

Jiang, H.X., Wang, Q.Y., Wang, H.Q., Chen, Y.F., Zhang, M.H., 2016. MOE-74 as an efficient catalyst for the low-temperature selective catalytic reduction of NO_x with NH_3. ACS Appl. Mater. Interfaces 8, 26817–26826.

Kan, J.W., Deng, L., Li, B., Huang, Q., Zhu, S., Shen, S.M., Chen, Y.W., 2017. Performance of Co-doped Mn-Ce catalysts supported on cordierite for low concentration chlorobenzene oxidation. Appl. Catal. A: Gen. 530, 21–29.

Liang, X.L., Liu, P., He, H.P., Wei, G.L., Chen, T.H., Tan, W., Tan, F.D., Zhu, J.X., Zhu, R. L., 2016. The variation of cationic microstructure in Mn-doped spinel ferrite during calcination and its effect on formaldehyde catalytic oxidation. J. Hazard. Mater. 306, 305–312.

Liu, P., He, H.P., Wei, G.L., Liang, X.L., Qi, F.H., Tan, F.D., Tan, W., Zhu, J.X., Zhu, R.L., 2016. Effect of Mn substitution on the promoted formaldehyde oxidation over spinel ferrite: Catalyst characterization, performance and reaction mechanism. Appl. Catal. B: Environ. 182, 476–484.

Liu, M., Li, C.T., Zeng, Q., Du, X.Y., Gao, L., Li, S.H., Zhai, Y.B., 2019. Study on removal of elemental mercury over MoO_3-CeO_2/cylindrical activated coke in the presence of SO_2 by Hg-temperature-programmed desorption. Chem. Eng. J. 371, 666–678.

Liu, J., Wang, J.W., Cheng, J., Zhang, Y.S., Wang, T., Pan, W.P., 2020. Distribution and emission of speciated volatile organic compounds from a coal-fired power plant with ultra-low emission technologies. J. Clean. Prod. 264, 121686.

Li, J.X., Xu, H.M., Liao, Y., Qiu, Y.X., Yan, N.Q., Qu, Z., 2020. Atomically dispersed manganese on a carbon-based materials for the capture of gaseous mercury: mechanism and environmental applications. Environ. Sci. Technol. 54, 5249–5257.

Li, D.D., Yang, G.L., Li, P.L., Wang, J.L., Zhang, P.Y., 2016. Promotion of formaldehyde oxidation over Ag catalyst by Fe doped MnOx support at room temperature. Catal. Today 277, 257–265.

Lochař, V., 2006. FT-IR study of methanol, formaldehyde and methyl formate adsorption on the surface of Mo/Sn oxide catalyst. Appl. Catal. A: Gen. 309, 33–36.

Ma, C.Y., Yang, C.G., Wang, B., Chen, C., Wang, F.B., Yao, X.L., Song, M.Y., 2019. Effects of H_2O on HCHO and CO oxidation at room-temperature catalyzed by MCo_2O_4 (M=Mn, Ce and Cu) materials. Appl. Catal. B: Environ. 254, 76–85.

Ma, Y., Zhang, G.K., 2016. Sepiolite nanofiber-supported platinum nanoparticle catalysts toward the catalytic oxidation of formaldehyde at ambient temperature: efficient and stable performance and mechanism. Chem. Eng. J. 288, 70–78.

Piumetti, M., Fino, D., Russo, N., 2015. Mesoporous manganese oxides prepared by solution combustion synthesis as catalysts for the total oxidation of VOCs. Appl. Catal. B: Environ. 163, 277–287.

Qie, Z.P., Sun, F., Zhang, Z.K., Pi, X.X., Qu, Z.B., Gao, J.H., Zhao, G.B., 2020. A facile trace potassium assisted catalytic activation strategy regulating pore topology of activated coke for combined removal of toluene/SO_2/NO. Chem. Eng. J. 389, 124262.

Qin, L., Zeng, G.M., Lai, C., Huang, D.L., Zhang, C., Xu, P., Hu, T.J., Liu, X.G., Cheng, M., Liu, Y., Hu, L., Zhou, Y.Y., 2017. A visual application of gold nanoparticles: simple, reliable and sensitive detection of kanamycin based on hydrogen-bonding recognition. Sens. Actuator B: Chem. 243, 946–954.

Raskó, J., Kecskés, T., Kiss, J., 2004. Formaldehyde formation in the interaction of HCOOH with Pt supported on TiO2. J. Catal. 224, 261–268.

Sato, A.G., Volanti, D.P., Meira, D.M., Damyanova, S., Longo, E., Bueno, J.M.C., 2013. Effect of the ZrO_2 phase on the structure and behavior of supported Cu catalysts for ethanol conversion. J. Catal. 307, 1–17.

Tang, W.X., Wu, X.F., Li, D.Y., Wang, Z., Liu, G., Liu, H.D., Chen, Y.F., 2014. Oxalate route for promoting activity of manganese oxide catalysts in total VOCs' oxidation: effect of calcination temperature and preparation method. J. Mater. Chem. A 2, 2544–2554.

Todorova, S., Kolev, H., Holgado, J.P., Kadinov, G., Bonev, C., Pereñíguez, R., Caballero, A., 2010. Complete n-hexane oxidation over supported Mn-Co catalysts. Appl. Catal. B: Environ. 94, 46–54.

Wang, X.Y., Kang, Q., Li, D., 2009. Catalytic combustion of chlorobenzene over MnO_x-CeO_2 mixed oxide catalysts. Appl. Catal. B: Environ. 86, 166–175.

Wang, J.L., Li, J., Zhang, P.Y., Zhang, G.K., 2018. Understanding the "seesaw effect" of interlayered K^+ with different structure in manganese oxides for the enhanced formaldehyde oxidation. Appl. Catal. B: Environ. 224, 863–870.

Wang, T., Li, C.T., Zhao, L.K., Zhang, J.Y., Li, S.H., Zeng, G.M., 2017. The catalytic performance and characterization of ZrO_2 support modification on CuO-CeO_2/TiO_2 catalyst for the simultaneous removal of Hg^0 and NO. Appl. Surf. Sci. 400, 227–237.

Wang, P., Wang, J., An, X., Shi, J., Shangguan, W., Hao, X., Xu, G., Tang, B., Abudula, A., Guan, G., 2021. Generation of abundant defects in Mn-Co mixed oxides by a facile agar-gel method for highly efficient catalysis of total toluene oxidation. Appl. Catal. B: Environ. 282, 119560.

Wang, L., Yue, H.Q., Hua, Z.L., Wang, H.Y., Li, X.B., Li, L.C., 2017. Highly active Pt/Na_xTiO_2 catalyst for low temperature formaldehyde decomposition. Appl. Catal. B: Environ. 219, 301–313.

Wang, T., Zhang, Y.S., 2019. Cases of ultra-low emission coal-fired power plants, in advances. In: Zhang, Y., et al. (Eds.), Ultra-Low Emission Control Technologies for Coal-Fired Power Plants. Woodhead Publishing Series in Energy, pp. 81–158.

Wu, H.Y., Li, C.T., Zhao, L.K., Zhang, J., Zeng, G.M., Xie, Y.E., Zhang, X.N., Wang, Y., 2015. Removal of gaseous elemental mercury by cylindrical activated coke with CoO_x-CeO_2 from simulated coal combustion flue gas. Energy Fuel 29, 6747–6757.

Xu, H.M., Qu, Z., Zong, C.X., Huang, W.J., Quan, F.Q., Yan, N.Q., 2015. MnOx/graphene for the catalytic oxidation and adsorption of elemental mercury. Environ. Sci. Technol. 49, 6823–6830.

Xu, Z.H., Yu, J.G., Jaroniec, M., 2015. Efficient catalytic removal of formaldehyde at room temperature using AlOOH nanoflakes with deposited Pt. Appl. Catal. B: Environ. 163, 306–312.

Yang, C.T., Miao, G., Pi, Y.H., Xia, Q.B., Wu, J.L., Li, Z., Xiao, J., 2019. Abatemnet of various types of adsorption/catalytic oxidation: a review. Chem. Eng. J. 370, 1128–1153.

Yan, Z.X., Xu, Z.H., Yang, Z.H., Yue, L., Huang, L.Y., 2019. Graphene oxide/Fe_2O_3 nanoplates supported Pt for enhanced room-temperature oxidation of formaldehyde. Appl. Surf. Sci. 467–468, 277–285.

Yan, Y.L., Yang, C., Peng, L., Li, R.M., Bai, H.L., 2016. Emission characteristics of volatile organic compounds from coal-, coal gangue-, and biomass-fired power plants in China. Atmos. Environ. 143, 261–269.

Yi, Y.Y., Li, C.T., Zhao, L.K., Du, X.Y., Gao, L., Chen, J.Q., Zhai, Y.B., Zeng, G.M., 2018. The synthetic evaluation of CuO-MnO_x-modified pinecone biochar for simultaneous removal formaldehyde and elemental mercury from simulated flue gas. Environ. Sci. Pollut. Res. 25, 4761–4775.

Yu, J.G., Li, X.Y., Xu, Z.H., Xiao, W., 2013. NaOH-modified ceramic honeycomb with enhanced formaldehyde adsorption and removal performance. Environ. Sci. Technol. 47, 9928–9933.

Zeng, J.W., Li, C.T., Zhao, L.K., Gao, L., Du, X.Y., Zhang, J., Tang, L., Zeng, G.M., 2017. Removal of elemental mercury from simulated flur gas over peanut shells carbon loaded with iodine ions, manganese oxides, and zirconium dioxide. Energy Fuel 31, 13909–13920.

Zhang, X.M., Deng, Y.Q., Tian, P.F., Shang, H.H., Xu, J., Han, Y.F., 2016. Dynamic active sites over binary oxide catalysts: In situ/operando spectroscopic study of low-temperature CO oxidation over MnO_x-CeO_2 catalysts. Appl. Catal. B: Environ. 191, 179–191.

Zhang, J.Y., Li, C.T., Zhao, L.K., Wang, T., Li, S.H., Zeng, G.M., 2017. A sol-gel Ti-Al-Ce-nanoparticle catalyst for simultaneous removal of NO and Hg^0 from simulated flue gas. Chem. Eng. J. 313, 1535–1547.

Zhang, G.K., Xiong, Q., Xu, W., Guo, S., 2014. Synthesis of bicrystalline TiO_2 supported sepiolite fibers and their photocatalytic activity for degradation of gaseous formaldehyde. Appl. Clay Sci. 102, 231–237.

Zhao, L.K., Li, C.T., Du, X.Y., Zeng, G.M., Gao, L., Zhai, Y.B., Wang, T., Zhang, J.Y., 2018. Effect of Co addition on the performance and structure of V/ZrCe catalyst for simultaneous removal of NO and Hg^0 in simulated flue gas. Appl. Surf. Sci. 437, 390–399.

Zhao, L.K., Li, C.T., Li, S.H., Wang, Y., Zhang, J.Y., Wang, T., Zeng, G.M., 2016. Simultaneous removal of elemental mercury and NO in simulated flue gas over V_2O_5/ZrO_2-CeO_2 catalyst. Appl. Catal. B: Environ. 198, 420–430.

Zhao, B., Yi, H.H., Tang, X.L., Li, Q., Liu, D.D., Gao, F.Y., 2016. Copper modified activated coke for mercury removal from coal-fired flue gas. Chem. Eng. J. 286, 585–593.

Zhou, F.S., Diao, Y.F., 2020. Magnetic copper-ferrosilicon composites as regenerable sorbents for Hg^0 removal. Colloids Surf. A: Physicochem. Eng. Asp. 590, 124447.

Zhou, J., Qin, L.F., Xiao, W., Zeng, C., Li, N., Lv, T., Zhu, H., 2017. Oriented growth of layered-MnO_2 nanosheets over α-MnO_2 nanotubes for enhanced room-temperature HCHO oxidation. Appl. Catal. B: Environ. 207, 233–243.

Zhu, X.B., Liu, S.Y., Cai, Y.X., Gao, X., Zhou, J.S., Zheng, C.H., Tu, X., 2016. Post-plasma catalytic removal of methanol over Mn-Ce catalysts in an atmospheric dielectric discharge. Appl. Catal. B: Environ. 183, 124–132.

Zhu, Z.Z., Lu, G.Z., Zhang, Z.G., Guo, Y., Guo, Y.L., Wang, Y.Q., 2013. Highly active and stable Co_3O_4/ZSM-5 catalyst for propane oxidation: effect of the preparation method. ACS Catal. 3, 1154–1164.

Zhu, L.L., Shen, D.K., Luo, K.H., 2020. A critical review on VOCs adsorption by different porous materials: species, mechanisms and modification methods. J. Hazard. Mater. 389, 122102.

Zhu, L., Wang, J.L., Rong, S.P., Wang, H.Y., Zhang, P.Y., 2017. Cerium modified birnessite-type MnO_2 for gaseous formaldehyde oxidation at low temperature. Appl. Catal. B: Environ. 211, 212–221.